

Decagonal Sn clathrate on *d*-Al-Ni-Co

Vipin Kumar Singh,<sup>1</sup> Eva Pospíšilová,<sup>2</sup> Marek Mihalkovič,<sup>2,\*</sup> Marian Krajčí<sup>2,†</sup>, Pramod Bhakuni,<sup>1</sup> Shuvam Sarkar,<sup>1</sup> Katariina Pussi<sup>3</sup>, D. L. Schlageel,<sup>4</sup> T. A. Lograsso,<sup>4</sup> Paul C. Canfield,<sup>4,5</sup> and Sudipta Roy Barman<sup>1,‡</sup>


<sup>1</sup>UGC-DAE Consortium for Scientific Research, Khandwa Road, Indore - 452001, Madhya Pradesh, India

<sup>2</sup>Institute of Physics, Slovak Academy of Sciences, Dúbravská cesta 9, SK-84511 Bratislava, Slovak Republic

<sup>3</sup>Department of Physics, School of Engineering Science, LUT university, FI-53851 Lappeenranta, Finland

<sup>4</sup>Ames Laboratory, Iowa State University, Ames, Iowa 50011, USA

<sup>5</sup>Department of Physics and Astronomy, Iowa State University, Ames, Iowa 50011, USA

 (Received 6 April 2022; revised 21 October 2022; accepted 14 December 2022; published 12 January 2023)

Decagonal quasiperiodic ordering of Sn thin films on *d*-Al-Ni-Co is shown based on scanning tunneling microscopy (STM), low-energy electron diffraction, and density functional theory (DFT). Interestingly, the decagonal structural correlations are partially retained even up to a large film thickness of 10 nm grown at  $165 \pm 10$  K. The nucleation centers called “Sn white flowers” identified by STM at submonolayer thickness are recognized as valid patches of the decagonal clathrate structure with low adsorption energies of these motifs. Due to the excellent lattice matching (to within 1%) between columns of Sn dodecahedra in the clathrate structure and pentagonal motifs at the *d*-Al-Ni-Co surface, the interfacial energy favors clathrate over the competing Sn crystalline forms. DFT study of the Sn/Al-Ni-Co composite model shows good mechanical stability, as shown by the work of separation of Sn from Al-Ni-Co slab that is comparable to the clathrate self-separation energy. The relaxed surface terminations of the  $R_2T_4$  clathrate approximant are in self-similarity correspondence with the motifs observed in the STM images from monolayer to the thickest Sn film.

DOI: [10.1103/PhysRevB.107.045410](https://doi.org/10.1103/PhysRevB.107.045410)

## I. INTRODUCTION

Quasicrystals show sharp diffraction spots although they do not have translational long-range order and rather possess forbidden rotational symmetries. In addition to intermetallic alloys [1,2], quasicrystallinity has also been observed in various forms such as colloidal systems [3], binary nanoparticle superlattices [4], molecular assemblies [5,6], chalcogenides [7], twisted bilayer graphene [8,9], and even in naturally occurring minerals [10]. Quasicrystals are fascinating, especially due to their unusual physical properties such as low specific heat, low thermal and electrical conductivities, and low friction [11–13], as well as evidence of Anderson localization [14], demonstration of pseudogap at the Fermi level [15], and recent prediction of topological states [16,17].

The basic entities that are known to form quasicrystals are clusters such as pseudo-Mackay and Bergman clusters [18]. Crystalline structures with cluster entities, for instance, clathrates, somewhat resemble the clusters that form the quasicrystals. The most straightforward rationalization of the bulk clathrate structure is via the network of its cage centers [19,20]. Polytetrahedral order [21,22] is the basis of the crystalline Frank-Kasper phases [19,20,23] and has been used in order to realize the structure of quasicrystals [24–26]. Materials exhibiting clathrate structure [27–33] have become a subject of interest due to their optical and thermoelectric properties [34,35], as well as due to their potential for

application [36,37]. Guest-free Si [38] and Ge [39] clathrates have wide quasidirect band gaps that are important for photovoltaic applications, and Sn with guest atoms has shown clathrate structures [40].

Since the last decade, Sn films have attracted considerable attention because of their interesting electronic properties [41–46]. In particular, in its single-layer honeycomb structure (stanene), Sn has been shown to exhibit topological properties [47–49]. In a recent advancement towards achieving elemental quasicrystal, we have shown using scanning tunneling microscopy (STM), low-energy electron diffraction (LEED), and density functional theory (DFT) that Sn can grow quasiperiodically up to about 4 nm thickness with a clathrate structure on *i*-Al-Pd-Mn substrate [50]. The clathrate quasiperiodic structure nucleates on *i*-Al-Pd-Mn because of an excellent matching (within 1%) of the cage-cage linkage length in Sn clathrates ( $\approx 1.26$  nm) with the pseudo-Mackay cluster-cluster separations in *i*-Al-Pd-Mn (1.255 nm).

In this study, we explore the growth of Sn films on decagonal (*d*)-Al-Ni-Co quasicrystal with a motivation to demonstrate the generality of the clathrate quasiperiodic structure of Sn. *d*-Al-Ni-Co has a different structure compared to *i*-Al-Pd-Mn: the former comprises of decagonal quasiperiodic planes, but exhibits translational periodicity along the tenfold (10f) axis with an interplanar distance of approximately 0.2 nm [51]. The structure of *d*-Al-Ni-Co has not been solved experimentally until date, but several models have been proposed in literature [52–54]. Sugiyama *et al.* determined the structure of the W approximant of *d*-Al-Ni-Co (W-Al-Ni-Co) using x-ray diffraction, and showed that it is closely related to *d*-Al-Ni-Co [54]. The 10f *d*-Al-Ni-Co surface was modeled by Krajčí *et al.* [55] based on W-Al-Ni-Co as alternating

\*marek.mihalkovic@savba.sk

†marian.krajci@savba.sk

‡barmansr@gmail.com

flat (*A*) and puckered (*B*) atomic layers perpendicular to the periodic axis along the *z* direction. The surface energy of *d*-Al-Ni-Co is reported to be  $1.17 \text{ J/m}^2$  [56], while that of Sn is  $0.71 \text{ J/m}^2$  [57]. Thus, from surface energy considerations, Sn is expected to wet the *d*-Al-Ni-Co surface. However, Sn deposition on *d*-Al-Ni-Co has been scarcely studied in literature. Shimoda *et al.* report a pseudomorphic monolayer of quasiperiodic Sn on *d*-Al-Ni-Co using RHEED, XPS, and STM [58]. For depositing Sn, these authors, however, precoated the backside of the specimen with Sn and then with heating Sn diffused and spread over to the front side. This method precludes possibility of growing thicker Sn films that – as we find in our work – requires low temperature.

Although there have been four decades of active research on quasicrystals, elemental quasicrystals have remained elusive so far. In this paper, we show the formation of decagonal Sn thin film (thickness  $< 1 \text{ nm}$ ) on a 10f *d*-Al-Ni-Co surface based on LEED and STM. The decagonal structural correlations are partially retained up to a large film thickness of 10 nm. The quasiperiodic motifs observed from STM up to 10 nm-thick Sn film are in good self-similarity correspondence with the decagonal clathrate  $\text{R}_2\text{T}_4$  approximant model of Sn calculated by DFT that show relaxed penta-hole and penta-cap terminations. The “Sn white flowers” (SnWFs) identified by STM after submonolayer Sn deposition are the nucleation centers of the decagonal clathrate structure with low adsorption energies. Due to the excellent lattice matching (to within 1%) between Sn clathrate and the *d*-Al-Ni-Co surface, the interfacial energy favors the clathrate. DFT study of the Sn/Al-Ni-Co composite model shows good mechanical stability, as shown by the work of separation of Sn from Al-Ni-Co slab that is comparable to the clathrate self-separation energy. The paper is organized as follows: We provide experimental evidence of decagonal quasicrystallinity in Sn thin films using STM and LEED (Sec. III A) and the evidence of decagonal structural correlations in the thick films is provided in Sec. III B. Thereafter, we provide a theoretical model for a decagonal clathrate structure of Sn from DFT (Sec. III C). A piece of evidence supporting the clathrate decagonal model is a detailed analysis of the nucleation supported by the STM results that are discussed in Sec. III D. Next, in Sec. III E, we consider a Sn/*d*-Al-Ni-Co  $\text{R}_2\text{T}_4$  approximant composite model to study the adlayer-substrate interaction with DFT. Finally, in Sec. III F we define the motifs based on our theoretical model and show that these are observed from STM and a sizable contiguous region of the image for the 10 nm-thick film is in reasonable agreement with the theory.

## II. METHODS

The STM experiments were carried out in a variable temperature STM system from Scientaomicron at a base pressure of  $5 \times 10^{-11} \text{ mbar}$ . The experiments were performed using an electrochemically etched polycrystalline tungsten tip that was cleaned *in situ* by  $\text{Ar}^+$  ion sputtering and voltage pulse method. The images were recorded in the constant current mode with the sample at ground potential for various sample bias voltages and are shown after low-pass Fourier transform filtering. The analysis was performed using the SPIP software. The zero of the color scale for all the STM images corresponds

to the bearing height, i.e., the most frequently occurring height. The root-mean-square roughness ( $S_q$ ) is defined as the square root of the sum of squares of each height value (*z*) at each pixel coordinate ( $x_k, y_l$ ) in the ( $M \times N$ ) pixel data set given by  $S_q = \sqrt{\frac{1}{MN} \sum_{k=0}^{M-1} \sum_{l=0}^{N-1} [z(x_k, y_l)]^2}$ .

The LEED equipment from OCI Vacuum Microengineering has a retractable four-grid rear view optics, and the patterns were recorded with a digital camera in nearly normal incidence geometry at 1 eV step of the beam energy ( $E_p$ ) that was varied from 30 to 200 eV. The *I*-*V* curves were determined by calculating the intensity of a LEED spot for each  $E_p$  in a window of fixed size with the spot in its middle. An averaging was performed for all the symmetry-equivalent spots. Image J software [59] was used to invert the gray color scale after applying the autocontrast option to adjust the brightness and intensity.

Monocrystalline *d*-Al-Ni-Co quasicrystal was grown from a high-temperature ternary melt [60] and separated from the excess liquid via centrifuging [61]. *d*-Al-Ni-Co was mounted on a specially fabricated cooling sample plate made of molybdenum. A smooth and clean *d*-Al-Ni-Co surface was obtained by cycles of 0.5–1.5 keV  $\text{Ar}^+$  ion sputtering and followed by annealing at 1043 K in the UHV chamber for 4 h [62]. Sn of 99.99% purity was evaporated using a water-cooled Knudsen evaporation cell [63] equipped with a shutter that is operated manually using a rotary feedthrough. The temperature of the cell used for deposition was 1163 K and this was measured by a K-type thermocouple placed at the outside bottom of the pyrolytic boron nitride crucible. The deposition was performed at an angle of  $70^\circ$  from the surface normal, and the pressure of the chamber during the deposition was  $5 \times 10^{-10} \text{ mbar}$ . The substrate surface was freshly prepared for both 0.2 and 1 ML Sn deposition. For the thick films with  $t_d$  varying from 3 to 37 min, the deposition was sequential. For the depositions at  $165 \pm 10 \text{ K}$ , the LEED was performed at the same temperature while STM was performed at 80 K.

Structural optimization study of the Sn surface terminations and reconstructions, as well as Sn/Al-Ni-Co model relaxations, have been performed using plane-wave DFT code Vienna *ab initio* simulation package (VASP) [64]. We used projector augmented wave potentials [65] in the PW91 generalized gradient approximation [66]. Default energy cutoff (ENCUT) 103.3 eV preset by “accurate” calculational setup turned out to be sufficient considering energy differences  $\Delta E$  between different samples: out of the four samples examined for convergence, change of the  $\Delta E$  from ENCUT = 103.3 to 300 eV was  $\leq 0.3 \text{ meV/atom}$ , certainly well below other unaccounted systematic inaccuracies. The *k*-point meshes were converged to comparable change in  $\Delta E$  upon increasing mesh density.

## III. RESULTS AND DISCUSSION

### A. Quasiperiodicity of Sn thin films ( $< 1 \text{ nm}$ ) on *d*-Al-Ni-Co

#### 1. Monolayer Sn

An STM topography image of 0.85 ML Sn on *d*-Al-Ni-Co in Fig. 1(a) indicates possible quasiperiodicity of the adlayer through sharp 10f spots in its fast Fourier transform (FFT) in Fig. 1(b) that has  $\sim 85\%$  contribution from the adlayer. The

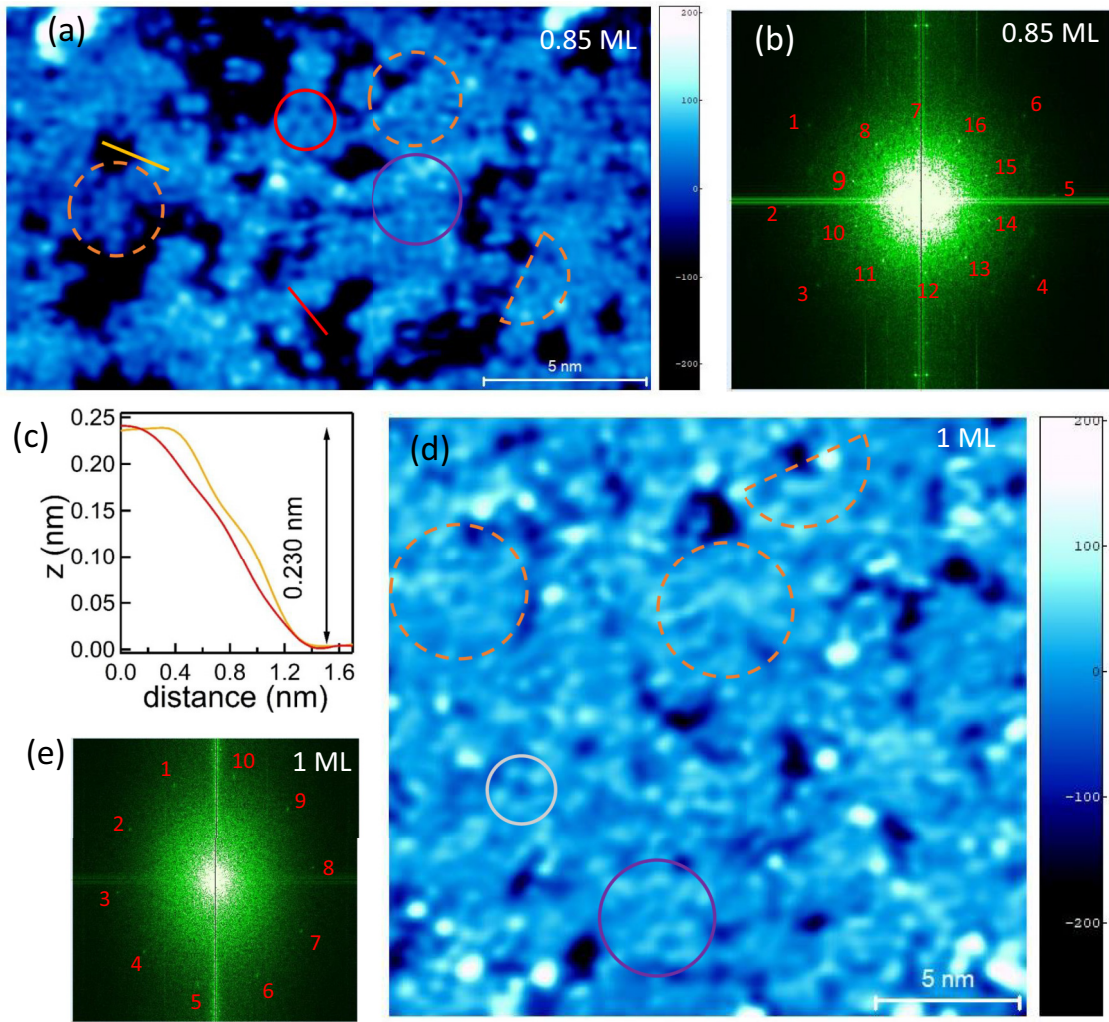


FIG. 1. (a) STM topography image of 0.85 ML Sn/*d*-Al-Ni-Co ( $I_T = 0.5$  nA,  $U_T = -1.5$  V) at 300 K. The color scale representing the height in picometers is shown on the right, zero corresponds to the bearing height. (b) Fast Fourier transform (FFT) of (a), the two sets of decagonal spots are numbered. (c) The height profile along the red and yellow lines in (a), the double arrow corresponds to the thickness of the Sn monolayer islands. (d) STM topography image ( $I_T = 0.6$  nA,  $U_T = -1.5$  V) of 1 ML Sn/*d*-Al-Ni-Co. In (a) and (d), the different motifs such as wheel (dashed orange circle), pentagon (gray circle), polygon assembly (violet circle), triplet (red circle), and crown (dashed orange half-circle) are highlighted. See Sec. III F and Fig. 15 for their description, same line type is used henceforth for highlighting the each type of motif. (e) FFT of (d) with the decagonal spots numbered 1–10.

FFT shows two sets of 10f spots. The spots are numbered such that the corresponding intensity profiles along the tangential direction can be shown. In Figs. S1(a) and S1(b) of the Supplemental Material (SM) [67], each intensity profile shows a peak at the position of the spot and thus all the spots are unambiguously identified. The ratio of their radii is  $1.92 \pm 0.03$ , which is close to  $\tau\chi = 1.90$ , where  $\tau$  is the golden mean given by  $\tau = (1 + \sqrt{5})/2 = 1.618$ .  $\chi$  is the ratio of the side of a regular pentagon and the distance from its center to a vertex; it is related to  $\tau$  by  $\chi = \sqrt{(3 - \tau)} = 1.176$  [68,69]. The outer set of spots is rotated by  $18^\circ$  with respect to the inner set. The height profiles taken along the red and yellow lines from the STM image [Fig. 1(a)] are plotted in Fig. 1(c). These show the difference of the average  $z$  corrugation (the double-sided arrow) of the Sn monolayer islands (light blue regions) and the substrate (dark), which is the thickness of the former under the assumption that the electronic height is equal to

the geometric height. After averaging over more than 30 such profiles from different parts of the image as in our earlier work [70], we find the thickness of the Sn monolayer to be  $0.23 \pm 0.02$  nm.

In Fig. 1(d), STM topography image of nearly one monolayer (0.97 ML) is displayed. The 10f symmetry of the spots observed in the FFT [Fig. 1(e)] and their intensity profiles along the tangential direction are shown in Fig. S1(c) of SM [67]. Two adjacent spots subtend an angle of  $36^\circ \pm 2^\circ$  at the center demonstrating the quasiperiodic nature of the Sn monolayer. Different quasiperiodic motifs of Sn such as wheel, crown, pentagon, triplet, and polygon assembly are highlighted in Figs. 1(a) and 1(d). These motifs are defined on the basis of the relaxed surface of the clathrate structural model calculated by DFT (see Sec. III F).

We find that the growth of Sn films of larger thickness beyond a monolayer is difficult at 300 K because of very low

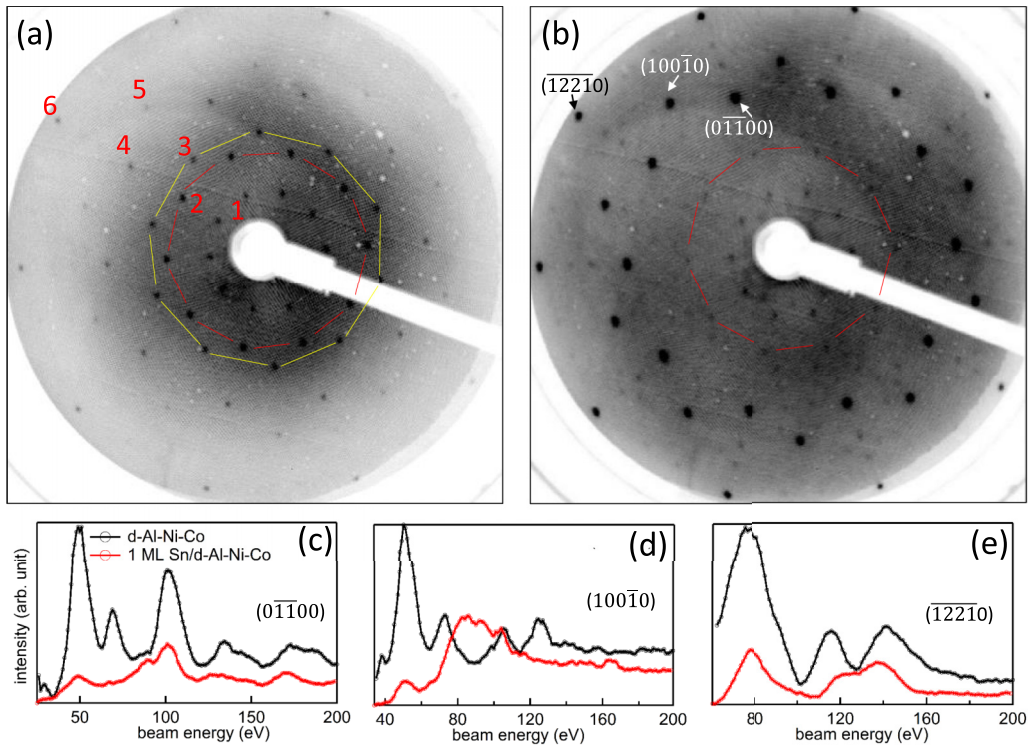


FIG. 2. The LEED pattern of (a) 1 ML Sn/*d*-Al-Ni-Co deposited at  $165 \pm 10$  K (LT) is compared to (b) the substrate *d*-Al-Ni-Co. Both the patterns are shown in an inverted grayscale and are taken with beam energy ( $E_p$ ) of 55 eV. The different sets of decagonal spots are numbered 1–6 in (a). The red and yellow lines highlight the second and the third set, respectively [the latter is not visible in (b)]. Comparison of the  $I$ - $V$  curves in the range  $30 \leq E_p \leq 200$  eV for (c)  $(0\bar{1}\bar{1}00)$ , (d)  $(100\bar{1}0)$ , and (e)  $(\bar{1}\bar{2}\bar{2}\bar{1}0)$  spots between 1 ML Sn and the substrate.

sticking coefficient and large diffusivity. On the other hand, at liquid helium temperatures, the diffusivity would be too low for an ordered growth. So, we have used an intermediate lower temperature (LT) of  $165 \pm 10$  K for growing Sn films thicker than a monolayer. LT is in fact a stringent requirement for growing Sn thick films.

The quasiperiodicity of the Sn monolayer at LT is evident from several sets of 10f spots in the LEED pattern (numbered 1–6) at an angular separation of  $36^\circ$  [Fig. 2(a)]. The ratios of the radii of the outer sets and the innermost set are related by powers and product of  $\tau$  and  $\chi$ , as shown in Table SI of SM [67]. The intensity profile through some of the spots (numbered 1–10) of both the substrate and the Sn adlayer is shown in Fig. S2 of SM [67]. To be noted is that the position of the spots changes with  $E_p$  (Fig. S3 of SM [67]). In particular, for  $E_p = 100$  eV, the prominent intensities are seen at a higher reciprocal distance compared to the substrate in contrast to  $E_p = 55$  eV (Fig. 2). Note that the LEED pattern is significantly different from the substrate: e.g., in Fig. 2(a), an extra set of diffraction spots (highlighted by yellow lines) is observed, which is not visible in *d*-Al-Ni-Co in Fig. 2(b). Also, the set of spots highlighted by red lines is more intense compared to the substrate. The shape of the intensity versus voltage ( $I$ - $V$ ) curves for the LEED spots as a function of  $E_p$  depends sensitively on the surface structure [71–74]. A comparison of the  $I$ - $V$  curves of monolayer Sn in Figs. 2(c)–2(e) for three different sets of spots shows that these are quite different from the substrate. For example, for the  $(0\bar{1}\bar{1}00)$  spot,

the substrate peak at 73 eV is completely absent, while the most intense peak at 52 eV is largely suppressed and shifted below 50 eV. It is a similar situation for the  $(100\bar{1}0)$  spot below 80 eV, and furthermore the 126 eV substrate peak is absent. For the  $(\bar{1}\bar{2}\bar{2}\bar{1}0)$  spot, the two peaks of the substrate at 116 and 141 eV move closer in the Sn layer and fill up the dip at 128 eV. The above discussed differences in the LEED evident from the patterns as well as the  $I$ - $V$  curves indicate that although the Sn monolayer exhibits decagonal symmetry, it has a different structure portraying a nonpseudomorphic growth.

A comparison of the STM topography image of the Sn monolayer at LT [Fig. S4(a) of SM [67]] with that at 300 K [Fig. 1(d)] shows that uniform wetting occurs at LT and their roughness is almost similar ( $S_q = 0.053 \pm 0.004$  nm at LT, whereas it is  $0.046 \pm 0.004$  nm at 300 K). Motifs such as wheel, crown, and polygon assembly are also observed [Figs. S4(b)–S4(d) [67]].

## 2. Sn film of 0.9 nm thickness

In Fig. 3(a), the  $t_d = 3$  min LEED pattern shows six sets of 10f spots at angular separation of about  $36^\circ$  that are similar to the Sn monolayer. In Fig. S5(a) of SM [67], the spots are numbered and the corresponding intensity profiles are shown in Figs. S5(b)–S5(e) [67]. A video file named as “0.9 nm” in the SM [67] shows that the intensities of all the spots in each set remain similar for the whole range of  $E_p$  i.e.,

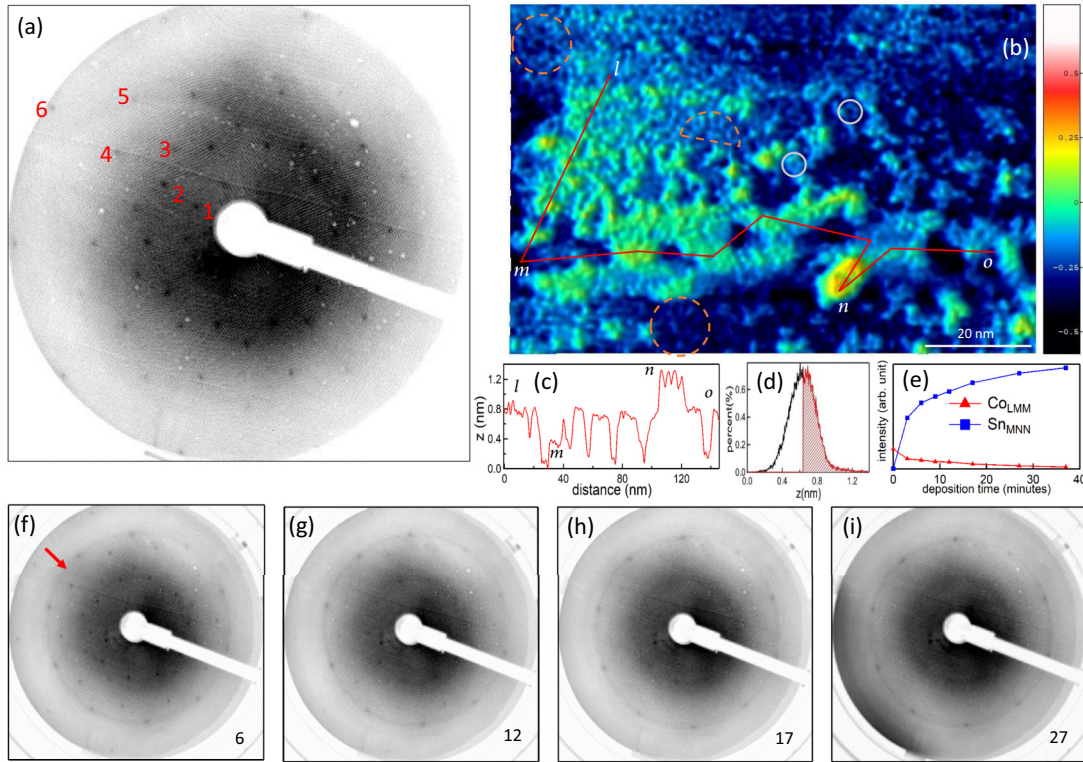


FIG. 3. (a) LEED pattern of a Sn thin film (0.9 nm thickness) deposited at LT on *d*-Al-Ni-Co. The pattern is shown in an inverted grayscale and is taken with  $E_p = 55$  eV, the different sets of decagonal spots are numbered as 1–6. (b) An STM topography image for the same deposition with  $I_T = 1.5$  nA,  $U_T = 1.5$  V. (c) The height profile along the line *lmno* shown by red color in (b). (d) The height histogram of (b). (e) Intensity variation of the Sn *MNN* and the Co *LMM* Auger signals as a function of  $t_d$ . (f)–(i) The LEED pattern Sn films deposited for  $6 \text{ min} \leq t_d \leq 27 \text{ min}$ , as shown at the lower right corner of each panel ( $E_p = 55$  eV).

$20 \leq E_p \leq 150$  eV. The above observations establish that this film exhibits decagonal symmetry. For comparison, the LEED video of the Sn monolayer is also included in the SM [67]. The ratios of the radii of the outer sets and the innermost set are related by powers and product of  $\tau$  and  $\chi$ , as shown in Table SII of SM [67].

A STM topography image of this film in Fig. 3(b) shows an increase in roughness with  $S_q$  being 0.15 nm. Motifs highlighted by dashed orange and gray circles exhibit resemblance with the monolayer. The crown and the wheel motifs [zoomed and compared with our theoretical model in Figs. S6(a) and S6(b)] are similar to those of the monolayer shown in Figs. 16(a) and 16(b). The STM image provides a measure of its thickness from the height profile along the line named as *lmno*, i.e., the red line in Fig. 3(a). It shows that there is considerable variation in the thickness and the maximum local height is  $\approx 1.2$  nm around *n* with respect to the region around *m* that has lowest height [Fig. 3(c)]. The height histogram of Fig. 3(d) is a nearly symmetric peak with maximum at 0.65 nm with 50% area (red shaded) having a thickness  $\geq 0.65$  nm. So, the peak position (0.65 nm) is considered to be the average thickness of the film referenced to *m*. Since the *d*-Al-Ni-Co surface is uniformly wetted by a monolayer of Sn, the thickness around *m* should be at least that of a monolayer, i.e., 0.23 nm. Thus, the average thickness of the intermediate layer is at least 0.88 nm (0.65+0.23 nm), i.e.,  $\sim 0.9$  nm.

## B. Sn thick films on *d*-Al-Ni-Co

### 1. Sn deposition for $6 \leq t_d \leq 27 \text{ min}$

Here, we first establish that there is a continuous increase of the average thickness of the Sn film with  $t_d$ . This is shown by the Sn *MNN* Auger signal that increases monotonically [Fig. 3(e)]. Concomitantly, the substrate related Co *LMM* Auger signal decreases and at  $t_d = 37$  min, it is almost in the noise level [Fig. 3(e)].

In Fig. 3(f), the LEED pattern for  $t_d = 6$  min with a thickness of 2 nm shows five sets of decagonal spots. The (100 $\bar{1}$ 0) spots also develop a continuous ring (red arrow), although the sets of spots at lower reciprocal distances do not show any such ring. At  $t_d = 12$ –27 min [Figs. 3(g)–3(i)], the spots at the lower reciprocal distances are diminished in intensity, whereas both the decagonal spots and the ring related to (100 $\bar{1}$ 0) are visible. The significance of the ring is discussed in the Sec. III B 2. The video files as a function of  $E_p$  corresponding to Figs. 3(f)–3(i) named as “6 min,” “12 min,” “17 min,” and “27 min,” respectively, are provided in the SM [67].

### 2. Thickest (10 nm) Sn film

A large area STM topography image of the largest thickness Sn film grown on *d*-Al-Ni-Co with  $t_d = 37$  min is shown in Fig. 4(a). The height profile in Fig. 4(b) along *pqrstuv* [red line in Fig. 4(a)] shows that the region around *s* (highlighted by a black rectangle) has a height of about 10 nm with respect

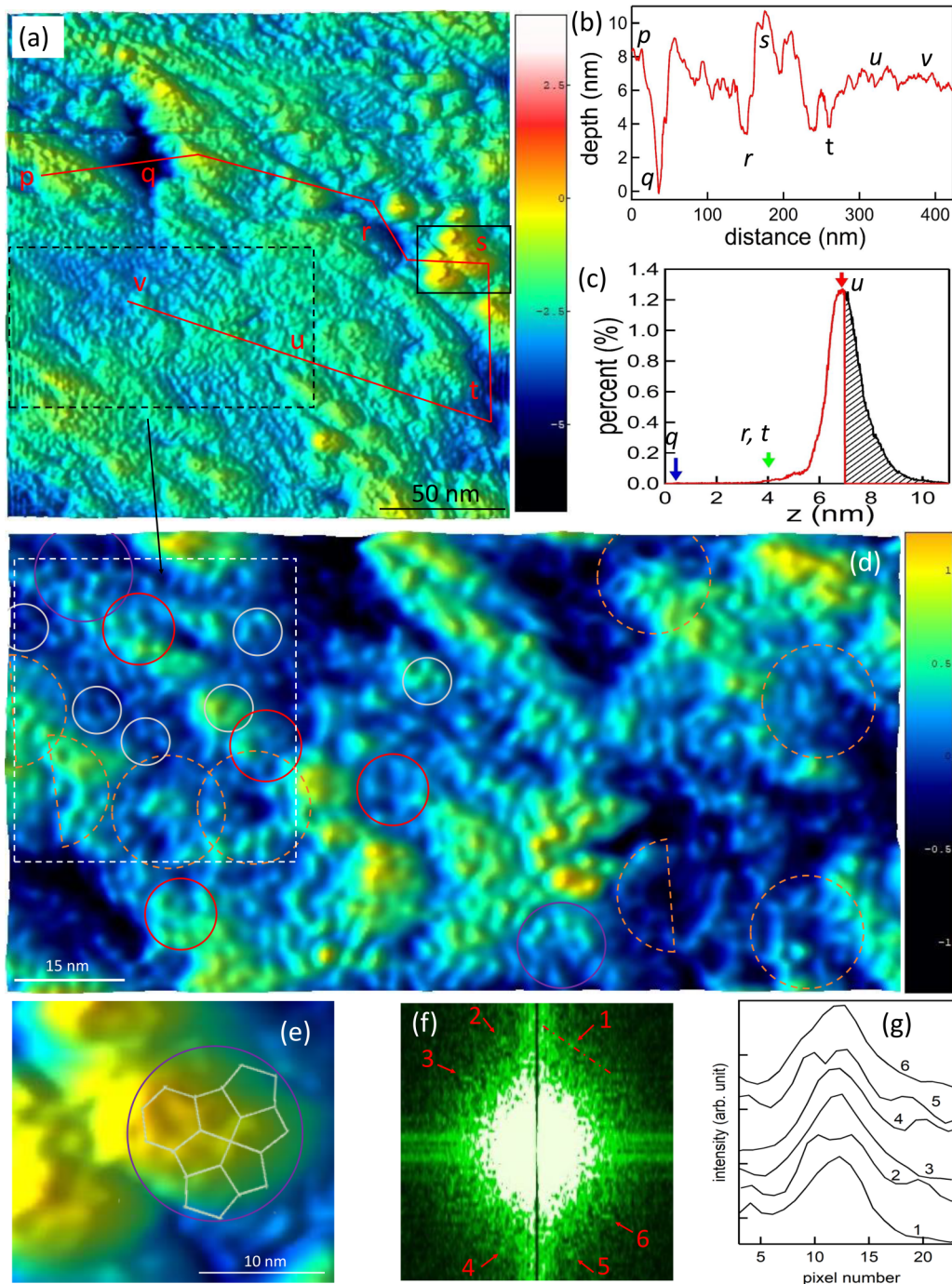


FIG. 4. (a) A large area STM topography image of a Sn thick film deposited for  $t_d = 37$  min on  $d$ -Al-Ni-Co for LT deposition ( $200 \text{ nm} \times 200 \text{ nm}$ ,  $I_T = 0.8 \text{ nA}$ ,  $U_T = 2 \text{ V}$ ). (b) The height profile along  $pqrstuv$  shown in red color in (a). (c) The height histogram of (a). (d) A  $121 \text{ nm} \times 62 \text{ nm}$  STM image from the dashed black rectangle in (a) showing motifs highlighted by colored circles as in Fig. 1. These motifs are defined by and compared with the approximant clathrate theoretical model in Sec. III F. (e) A zoomed image of the largest thickness ( $\approx 13 \text{ nm}$ ) region around  $s$  enclosed by a black rectangle in (a). (f) FFT of the Sn thick film with the spots indicated by red arrows and numbered 1–6. (g) Intensity profiles of the FFT spots along the tangential direction (as shown by a red dashed line for spot 1) shown staggered along the vertical axis.

to the local minimum region (e.g., region  $q$ ). However, the heights exhibit substantial lateral variation, e.g., around  $p$  it is  $8 \text{ nm}$ , whereas in a large region around  $uv$  it is  $6\text{--}7 \text{ nm}$ . Thus, the film exhibits a rugged topography that resembles a geographical undulated “hilly terrain,” where a valley represents the local minimum region ( $q$ ), but the bottom of the valley is at

a considerably larger height compared to the “sea level” (i.e., the monolayer). To find its average thickness, we consider a uniform Sn deposition with time: thus, for  $t_d = 37 \text{ min}$  the estimated thickness at  $q$  region is about  $2.8 \text{ nm}$ . This is estimated on the assumption that for the  $0.9 \text{ nm}$  film grown with  $t_d = 3 \text{ min}$ , the thickness of the minimum region [ $m$  in

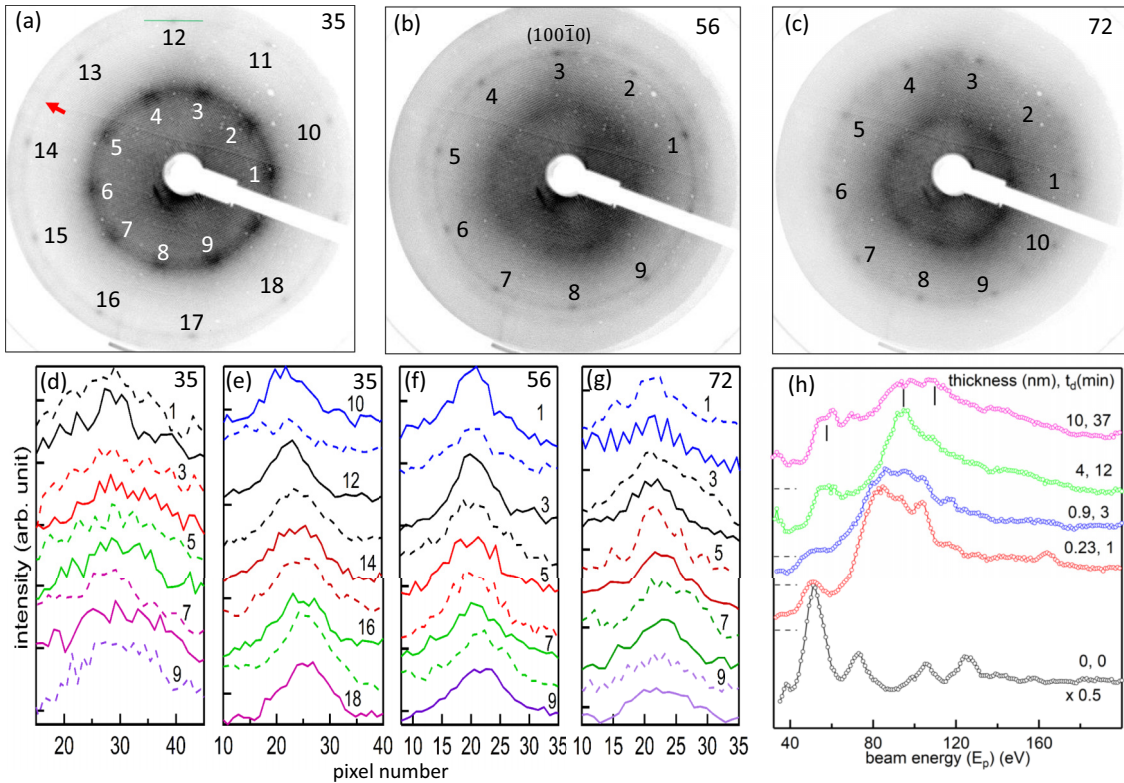


FIG. 5. LEED patterns of the 10 nm-thick Sn film recorded with  $E_p =$  (a) 35 eV, (b) 56 eV, and (c) 72 eV shown in an inverted scale. The intensity profiles along the tangential direction [e.g., along green line in (a) for spot 12] through the spots (d) 1–9 and (e) 10–18 in (a); (f) 1–9 in (b); (g) 1–10 in (c). (h) The  $I$ - $V$  curves corresponding to the  $(100\bar{1}0)$  spot for films of different thickness and  $t_d$  shown staggered along the vertical axis, the zero for each shown by dashed horizontal lines.

Fig. 3(b)] is one monolayer (0.23 nm). This estimate of the thickness at  $q$  is consistent with the fact that the substrate Co Auger signal is almost completely suppressed [Fig. 3(e)]. Note that the total area of regions having thickness close to  $q$  is only 1%–2% of the whole area of the film. In Fig. 4(c), the height histogram shows a nearly symmetric peak centered at 7 nm ( $\approx 50\%$  of the area shown by black shading has a thickness  $\geq 7$ ) that is taken as the average thickness with respect to  $q$  whose thickness is 2.8 nm. Thus, by adding these two numbers, the average thickness turns out to be  $10 \pm 0.5$  nm.

This film has an order of magnitude larger roughness ( $S_q = 0.54$  nm) compared to the monolayer ( $S_q = 0.053$ ). In spite of this, the characteristic motifs similar to those observed for the thin films are noticed [Fig. 4(d)]. The largest thickness region around  $s$  portrays an elevated dome highlighted by a violet circle in Fig. 4(e), whose average base diameter is  $12 \pm 3$  nm, as shown by the histogram in Fig. S7 of SM [67]. It is interesting to note that a quasiperiodic motif is observed on the dome, which partially resembles a polygon assembly (see Sec. III F).

In Fig. 4(f), an averaged FFT of the STM images shows occurrence of 6 spots (1–6). Their presence is established in Fig. 4(g) by the intensity profiles across the spots along the tangential direction (as shown for spot 1 by a red dashed line). It may be noted that a notional circle joining the spots is distorted to an oval shape, which could be related to the thermal drift in the STM measurement [50]. The spots are

weaker compared to that of the monolayer, as also in the case of the LEED spots shown in Fig. 5. Possible reasons for this could be the intrinsic puckered nature of the film (as shown in Sec. III F), stochastic processes, competing disorder, and the roughness of the film due to growth at LT that degrades the quality of the STM images.

LEED investigation of the Sn thick film shows 10f spots highlighted by numbering in Figs. 5(a)–5(c), and their intensity profiles are shown in Figs. 5(d)–5(g). A peak representing each spot is clearly observed with respect to the background, and these decagonal spots provide the evidence of the decagonal symmetry in the thick film. At  $E_p = 35$  eV, the outer set of spots are  $18^\circ$  rotated with respect to the inner spots [Fig. 5(a)], and ratio of the radii of the outer spots (10–18) and the inner spots (1–9) is 1.86 ( $\approx \tau\chi = 1.9$ ). Any possibility of crystalline domains [75] or presence of approximant phases are ruled out because there are no extra spots or splitting of the spots at any  $E_p$  (also see the video file named “10 nm” in SM [67]). All the spots move towards the (0,0) spot as  $E_p$  increases. It may be noted that aside from the discrete spots, as in Figs. 3(f)–3(i), a weak continuous ring that joins the  $(100\bar{1}0)$  spots is observed [red arrow in Fig. 5(a)] possibly indicating a rotational degree of freedom between the decagonal structures. The latter could probably be related to its clathrate structure since Engel *et al.* proposed possibility of random tiling quasicrystal in clathrates that are axially symmetric [76]. However, this would mean that the intermediate regions connecting the decagonal structures would not be periodic.

In Sec. III F (Fig. 17), we discuss this further by comparing the STM image of the 10 nm film with DFT based decagonal clathrate model that is presented in the Sec. III C.

The  $I$ - $V$  curve for the (100 $\bar{1}$ 0) spot of the Sn thick film exhibits peaks centered at  $E_p = 58, 95,$  and  $110$  eV, as shown by the ticks in the top curve of Fig. 5(h). The peak positions are similar to the 4 nm film ( $t_d = 12$  min), although in the latter, the 95 eV peak is somewhat more intense. The peaks in  $I$ - $V$  curves of the thin films [0.23 nm, i.e., one monolayer and 0.9 nm in Fig. 5(h)], although have nearly similar shape, are shifted by about 8–15 eV towards lower  $E_p$ , which implies a possible change in the lateral length scale [77]. Finally, it is noteworthy that the shape of the  $I$ - $V$  curves of the Sn films of different thicknesses starting from the monolayer (0.23 nm) are completely different from those of the substrate that has the peaks at  $E_p = 52, 73, 106,$  and  $125$  eV. This shows that the structure of the Sn films, although decagonal, is different from the substrate.

### C. Model for the atomic structure, surface termination, and DFT-optimized reconstruction of the Sn decagonal clathrate

The low-temperature stable phase of Sn, the  $\alpha$ -Sn in cubic diamond  $sp^3$ -bonded structure (“gray tin”), transforms to metallic and denser tetragonal  $\beta$ -Sn (“white tin”) above  $\sim 286$  K. The clathrate structures are also  $sp^3$  bonded by grouping atoms around point centers into empty cages. In our experiments, the thick Sn film was deposited at  $\sim 165$  K, deeply in the stability range of  $sp^3$ -bonded structures. At zero temperature, the cohesive energy differences of the alternative candidates for stability relative to  $\alpha$ -Sn obtained from DFT are +46 meV/atom for the  $\beta$ -Sn and +29 meV/atom for the face-centered-cubic clathrate type II [that contains highest fraction of the smallest dodecahedral cages and has lowest energy out of all clathrates (see Ref. [50] for a discussion about type II and III clathrates)]. Given the fact that the  $d$ -Al-Ni-Co substrate surface exhibits excellent match with the clathrate structure (see Sec. III D), nucleation of the  $\alpha$ -Sn and  $\beta$ -Sn structures must be suppressed due to the surface structure incompatibility. Moreover, the low deposition temperature is another disadvantage factor for metallic  $\beta$ -Sn. Presumably, an *amorphous* Sn phase might compete with the magic clathrate interfacial compatibility with  $d$ -Al-Ni-Co. But, while Si or Ge amorphous phases can be prepared easily and they have apparently  $sp^3$ -bonding nature, reports on amorphous Sn are very scarce, and to our knowledge literature does not report  $sp^3$ -bonded, low-density amorphous Sn phase that might be a hypothetical competitor at low temperatures.

In addition to these general considerations, the clearly recognizable *decagonal* symmetry of the LEED pattern from the thick Sn layer rules out any of the alternatives considered above. The role of the substrate is to prevent possible formation of crystalline Sn structures. In the following, we develop detailed theoretical, although indirect, support for *decagonal clathrate* as the only plausible candidate model structure for the thick Sn film. In Sec. III C 1, we argue how the decagonal clathrate follows from the dual relationship (where connecting the centers of the faces of one structure gives the other, e.g., an icosahedron gives a dodecahedron) between the Frank-Kasper and the clathrate structures [19,20,78]. We then review the

decoration prescription associating the precise bulk clathrate atomic structure of Sn with two-dimensional geometry of the R-T tilings. Section III C 2 discusses the decagonal clathrate surface terminations, and finally Sec. III C 3 reports on the DFT-guided energy optimization of such terminations by adding adatoms at specific locations to neutralize the energy cost of the unsaturated bonds at the surface.

#### 1. Tiling description of the decagonal clathrate

Frank and Kasper [19,20] pointed out that the network of clathrate cage centers forms tetrahedrally close-packed (TCP) geometry, and suggested that new clathrate structures can be derived from the known examples of the metallic structural family. Following this route, a decagonal TCP quasicrystal structure [79] can be dual transformed into *decagonal clathrate* [50]. The common geometrical framework of the two related structural families is decagonal tiling of rectangles and isosceles triangles (R-T tiling hereafter).

The decagonal R-T tiling, common geometry for metallic TCP structures or clathrates, consists of isosceles triangles (T) with two shorter sides with length  $a$  and a longer side  $b = a\sqrt{\tau} + 2/\tau$  and rectangles (R) with aspect ratio of  $\sqrt{\tau} + 2/\tau$ . In a random R-T tiling, R or T tiles pack without restrictions by sharing  $a$  or  $b$  edges. DFT-optimized tile edge lengths for the clathrate structure are  $a = 1.082$  nm and  $b \approx 1.268$  nm. Wider angle of the T tiles is  $2\pi/5$  so that five T's pack around a common vertex implementing a local fivefold symmetry. R-T tiling is *bipartite* since tiling vertices can be uniquely partitioned into “even” and “odd” via a simple rule: pairs of vertices connected by  $a$ -type linkage must have opposite parity. Decagonal R-T tiling has a close relationship with tilings of Ammann rhombuses: T tile is exactly half of the “fat” rhombus, and the R tile connected via  $b$ -type edge with T tile corresponds to a pair of  $36^\circ$  skinny rhombs, plus a T tile.

Given an R-T tiling, the backbone of the decagonal clathrate structure ( $\sim 85\%$  of the atoms) is given just by columns of dodecahedral cages centered around tiling vertices, as illustrated in Fig. 6(a). The dodecahedra forming the column are stacked on the top of each other, defining vertical stacking period of  $c = 2d_{\text{dod}} \approx 1.251$  nm, where  $d_{\text{dod}}$  is the shorter face-to-face diameter of the dodecahedron. The columns possess *local* 10f screw symmetry axes  $10_2$ , and the nearby columns related by translation over  $a$ -type edges are mutually rotated by  $2\pi/10$ , implementing the bipartiteness property.

The dodecahedron columns can be also viewed as stackings of “puckered” 10-rings and “flat” pentagons. Figures 6(b)–6(e) illustrate how this column decomposition invokes *layering* of the structure: the 10-rings give rise to strongly puckered  $P$ -type layers, while pentagons are always located at singular height in “flat”  $F$ -type layers. Full stacking period then reads as  $FPF'P'$ , where the primed layer (10-rings or pentagons) are related to the nonprimed motifs by action of the local  $10_2$  screw axis associated with every vertex column:  $2\pi/10$  rotation combined with half-period translation. The four stacking-period layers are centered at fractional heights  $z = 0$  ( $F$ ),  $\frac{1}{4}$  ( $P$ ),  $\frac{1}{2}$  ( $F'$ ), and  $\frac{3}{4}$  ( $P'$ ), respectively. While  $F$ -type layers occur at single discrete heights, the  $P$ -type layers span significant width of  $3.2 \text{ \AA}$ , measured from the topmost



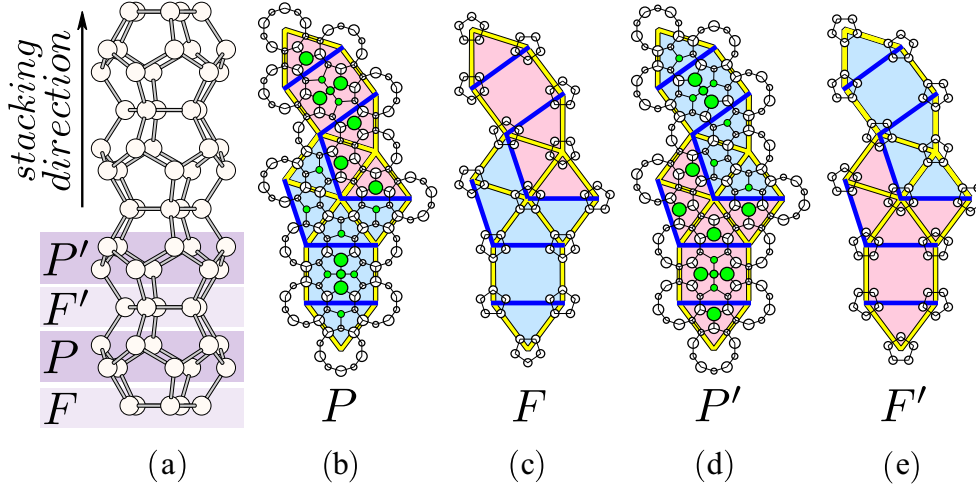


FIG. 6. (a) Side view of the column of stacked dodecahedra, decorating the vertices of the R-T tiling, the stacking direction  $z$  perpendicular to the substrate surface is indicated by a vertical arrow, its length corresponds to the stacking period  $c$  ( $= 1.251$  nm). Top view of the layer-by-layer decomposition of one repeat ( $PFP'F'$ ) of the bulk structure for a small patch of the R-T tiling, where the layers are denoted by (b)  $P$ , (c)  $F$ , (d)  $P'$ , and (e)  $F'$ . Open circles are Sn atoms that belong to the columns of the dodecahedra. Green circles are “interstitial” Sn atoms outside the columns of stacked dodecahedra. The sizes of the circles representing the atoms scale with their vertical height.

to the bottommost  $P$ -layer atom. Separation from a topmost  $P$ -layer atom to the  $F$ -layer plane is  $1.5$  Å.

The “decoration rule” is completed by placing “interstitial” atoms outside the dodecahedral columns; these are shown as green filled circles in Figs. 6(b)–6(e). Upon placing the interstitial atoms, every Sn atom in the structure satisfies  $sp^3$ -bonding constraints: the coordination is strictly four, and the bond angles vary within  $105^\circ$ – $120^\circ$  (compared to  $\approx 109.5^\circ$  bond angles in the  $\alpha$ -Sn diamond structure).

The symmetry relationships between local atomic motifs are conveniently represented by tile coloring: both R and T tiles are either pink, or light blue, depending on the orientation of pentagons in the  $F$  and  $F'$  layers.  $P/P'$  layer projected atomic positions are the same for either tile coloring, but their vertical displacements from the  $z = \frac{1}{4}$  or  $\frac{3}{4}$  fractional heights [reflected by circle sizes in Figs. 6(b)–6(e)] are opposite for the pair of colored tiles.

Table I summarizes the atomic content of the R and T tiles. In case of decagonal tiling, number frequency ratio of the T to R tiles is  $4\tau$ , and the respective tile areas are  $S_T = a^2\sqrt{\tau+2}/4$  and  $S_R = a^2\sqrt{\tau+2}/\tau$ ; hence, coverage contribution  $\rho_\alpha$  in the decagonal structure will be  $0.427$   $ML_\alpha$  for  $F$ -type and  $1.085$   $ML_\alpha$  for  $P$ -type layers.

TABLE I. The atomic content of R and T tiles averaged over primed and nonprimed layers.  $N_{\text{at}}$  gives the number of Sn atoms per respective tile, and  $\rho_\alpha$  is the coverage expressed in units of the (111)-type  $\alpha$ -Sn monolayer  $ML_\alpha$ .

	Triangle (T)		Rectangle (R)	
	$F$	$P$	$F$	$P$
$N_{\text{at}}$	5/2	6	5	15
$\rho_\alpha$ ( $ML_\alpha$ )	0.4507	1.0816	0.3646	1.0938

In their pure forms, the decorated R and T tilings exactly correspond to the well-known canonical clathrates composed from four canonical cages, entirely filling the space. In particular, the pseudo-10f axis is parallel to the cubic (110) direction in clathrate type II structure revealing isosceles triangles geometry, and to (100) direction in type III hexagonal clathrate showing pure-R tiling. Figure 7 shows a large decagonal clathrate “approximant” with  $10.25$  nm  $\times$   $8.72$  nm  $\times$   $1.25$  nm sides of the periodic cell, in which R and T tiles pack together to form eventually large pentagonal motifs. Inset in the upper left corner of the panel shows (pseudo)-10f zeroth layer of the diffraction pattern: deviation from perfect decagonal symmetry is hardly visible.

## 2. Decagonal clathrate: Surface terminations

We require that a proper Sn clathrate termination, in analogy with  $\alpha$ -Sn diamond surfaces, leads to at most one unsaturated bond for any atom exposed on the surface, i.e., the coordination number is  $\geq 3$ . Optimization strategy based on this assumption proved successful in predicting clathrate structures of reconstructed, free-standing ultrathin slabs as a ground state between  $2.5$ – $7$   $ML_\alpha$  thickness for Si and Ge, and for  $5$ – $8$   $ML_\alpha$  thick Sn slabs [80]. Here, we define “thickness” or coverage in units of (111)-type monolayer of the diamond structure ( $\alpha$ -Sn in case of tin). Note that our experimental film thickness is derived from the height coordinate, hence, it is not directly connected with  $ML_\alpha$  units used in this section.

It turns out that straight planar cuts normal to the stacking direction are valid surface terminations, satisfying the coordination-number requirement, for cuts at heights in-between layers defined in Fig. 6. Atoms exposed to the surface are always from two topmost layers  $P + F$  or  $F + P'$  or, in short,  $PF$  or  $FP'$  layers. Termination by  $F'P$  or  $FP'$  bi-layers with  $P/P'$  on the top exhibits 10-rings centered on the stacked dodecahedra column axis, at the tiling vertices.

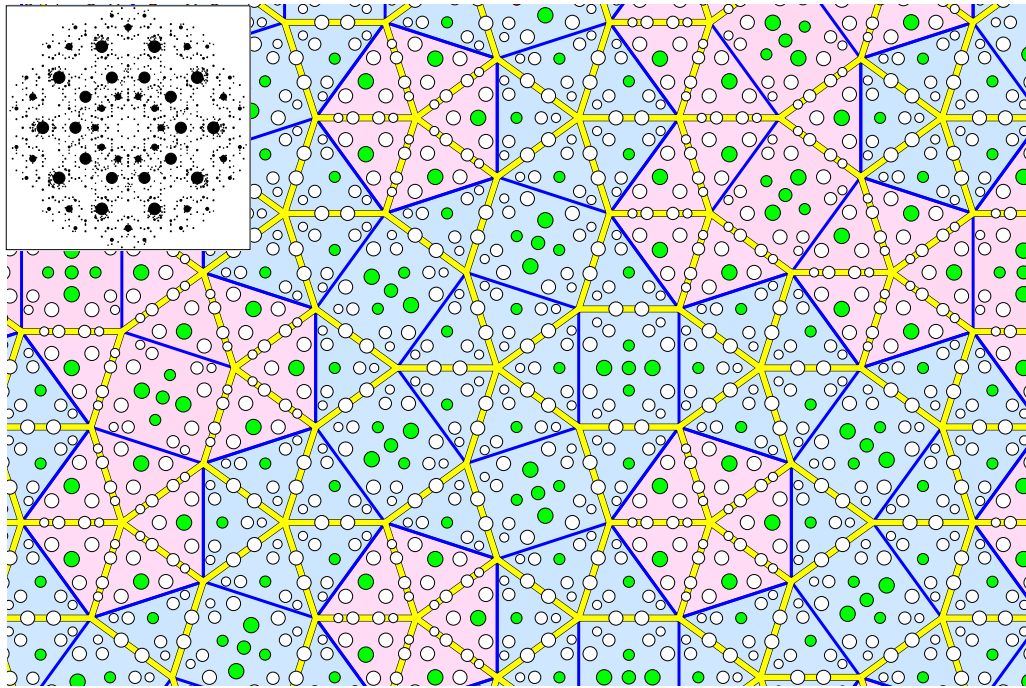


FIG. 7. Fragment of a large decagonal approximant with 2692 atoms per cell showing a  $PF$ -bilayer slice, surface perpendicular to the pseudo-10f axis. Tile coloring as in Fig. 6; also note that superposition of Figs. 6(b) and 6(c) gives the bilayer slice shown here for a much bigger continuous tiling fragment. The inset shows the diffraction pattern of the approximant structure parallel to the stacking  $c$  direction, revealing nearly perfect 10f symmetry.

Termination by  $PF$  or  $P'F'$  bilayer (with topmost  $F$  layer) places pentagonal caps on the top of the 10-rings, thus closing the dodecahedral cages at the surface.

Figure 8 depicts the two possible terminating surfaces for each kind of the tile on the surface: T or R tiles with topmost layer  $P$  are designated  $T_h/T'_h$  and  $R_h/R'_h$ , respectively, for the

two flavors of each tile. Atoms represented by yellow circles with a blue circular spot at the center are 3-coordinated atoms that possess one unsaturated bond each. The edge markings (green crosses/rectangles for yellow  $a$ -type linkages, blue triangles for  $b$ -type linkages) implement tile packing rules for valid clathrate decorations.

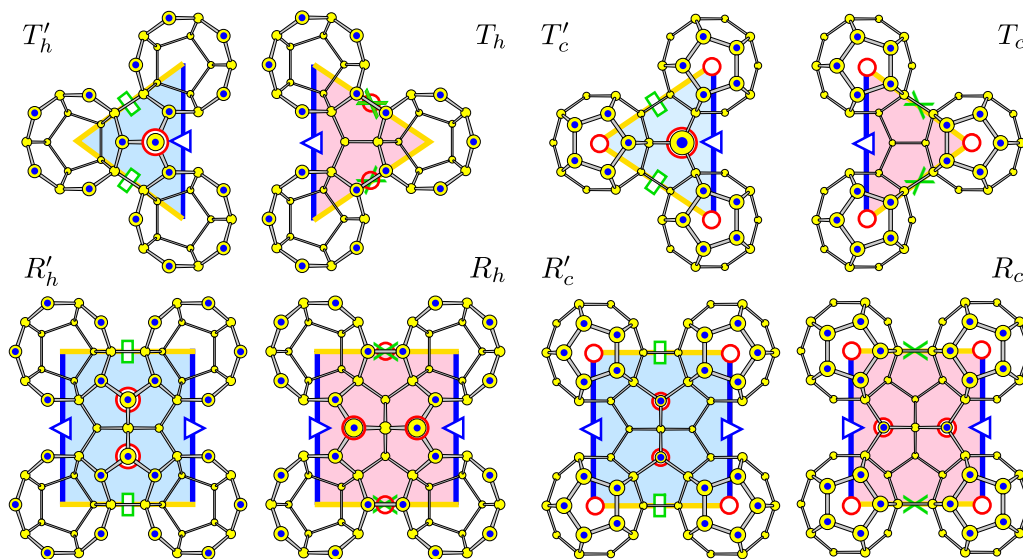


FIG. 8. Tile-decoration rule for T and R tiles shown in the top view. Edge markings (green crosses and rectangles, blue triangles) implement “packing rule” for edge sharing in a tiling. The tiles on the left side of the vertical line with terminations just above  $P$ -type layers with 10-rings are subscripted with letter “ $h$ ” (hole), while those on the right with  $PF$ -type termination with “penta-caps” on the top of 10-rings are labeled with subscript “ $c$ .” All Sn atoms are represented by yellow circles, atoms marked by blue circular spots in the center are 3-coordinated (before reconstruction). Red circles mark energy-minimizing adatom positions.

*Comparison with diamond structure (111)-type termination and clathrate growth.* The unreconstructed (111)-type diamond surface of Sn shows puckered even-odd honeycomb lattice with even and odd sites located at two nearby planes, that are  $\sim 1$  Å apart from each other. The topmost sublayer exposes 3-coordinated atoms while bottom sublayer atoms are 4-coordinated. Hence, 50% of the atoms on the surface have unsaturated bonds.

In case of clathrate Sn,  $P$  or  $P'$  terminating layers provide  $1.09 \text{ ML}_\alpha$  coverage (where  $\text{ML}_\alpha$  refers to diamond-111 surface layer), out of which  $0.53 \text{ ML}_\alpha$  atoms are 3-coordinated, the fraction  $\frac{0.53}{1.09} \approx 0.486$  is very similar to the diamond structure. However, capping the 10-rings by 5-caps in another growth stage adds another  $0.43 \text{ ML}_\alpha$  coverage, while *keeping the number of 3-coordinated atoms constant*. Thus, the  $PF$  (or  $P'F'$ ) bilayers terminated by 5-caps of the  $F$ -type layers add  $1.52 (1.09+0.43) \text{ ML}_\alpha$  of the coverage, out of which less than 35% of atoms have unsaturated bonds, appreciably less than in the case of diamond. Width of one such bilayer is  $\geq 6$  Å, about the same as two (111) layers of the diamond structure.

Since the 10-ring centers are laterally separated by  $a$  or  $b$  linkages ( $\sim 1$ – $1.2$  nm) shown as yellow or blue tile edges in Fig. 6, capping the 10-rings by 5-caps proceeds independently from one column of dodecahedra to another, which presumably precludes “layer-by-layer” growth mode. This is not surprising because of the three-dimensional (3D) character of the clathrate fundamental units: cages. On the other hand, cages can be viewed as a local, relatively stable unit in which Sn atoms are not less than 3-coordinated even when the cage is entirely isolated. The unsaturated bonds on the cage surface then act effectively as attractive potential, coalescing the cages together while saturating the bonds, and minimizing the surface area during growth. We expect that the growth mode of the Sn clathrate will be either pure island or mixed island-layer type, depending on the energy scales related to processes of (1) completion of a surface cage and (2) coalescing cages together.

To summarize, in our idealized model the clathrate growth proceeds in two stages: building mutually interconnected network of the  $P$ -layer atoms exhibiting nearly equal number of unsaturated bonds per surface atom as the diamond structure (111) surface, while in the second stage the 10-rings are covered by 5-caps in a stochastic process proceeding randomly and independently at any location on the surface.

### 3. Surface reconstruction

Terminations of  $sp^3$ -bonded surfaces necessarily produce unsaturated dangling bonds with significant energetic cost; the latter can be reduced by appropriately positioned “adatoms” that do not occupy generic lattice positions. In this subsection, we explore adatomic modifications of the clathrate surface structure by minimizing DFT surface energies.

As an example, let us first consider (111)-type surface termination of the related  $sp^3$ -bonded  $\alpha$ -Sn diamond structure, illustrated in Fig. 9 on the example of so-called  $\sqrt{3} \times \sqrt{3}$  reconstruction. The unreconstructed surface (i.e., without the red colored adatoms) is built up from 3-coordinated orange-colored Sn atoms in the upper half-layer of the honeycomb lattice, while the yellow 4-coordinated Sn atoms appear  $\sim 1$

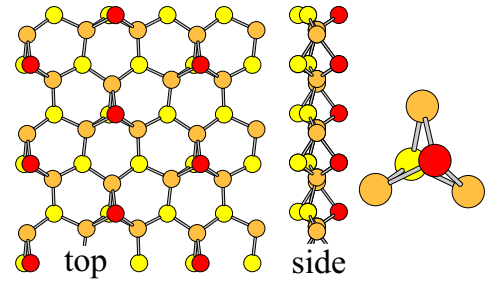


FIG. 9. Top and side views of the  $\sqrt{3} \times \sqrt{3}$  reconstruction of the diamond  $\alpha$ -Sn(111) surface: adatoms are shown in red, 3-coordinated Sn atoms (become 4-coordinated *after* adatom placement) are orange, and fully 4-coordinated Sn atoms are yellow. Yellow atoms represent the topmost bulk layer. *Right*: the dumbbell motif.

Å below. The yellow (orange) coloring divides the underlying honeycomb lattice into even (odd) parts. Its surface energy  $\Gamma$  decreases from 41 to 33 meV/Å<sup>2</sup> after positioning the Sn “adatoms” above some of the 4-coordinated atoms: they are shown in red color in Fig. 9, and the “top” view is slightly off the surface normal to make the yellow atoms visible. The placement of adatoms leads to formation of 5-atom *dumbbell* motifs enlarged in the rightmost panel of the figure. The remarkable aspect of this scenario is that the adatom (red in the figure) forms *lateral*, 2.9-Å-long bonds with three nearby 3-coordinated orange Sn atoms, while being positioned 3.4 Å above the 4-coordinated yellow atom, leading to three  $\sim 60^\circ$  bond angles between the orange-red and orange-yellow Sn atom bonds. Apparently, the advantage of saturating the lateral bonds exceeds the disadvantage from introducing the  $\sim 60^\circ$  bond angles.

Clathrate surfaces do not offer any exactly analogous configurations of the 3-coordinated atoms on the surface. Since the majority of the facets bounding the clathrate cages appearing on the surface are *pentagons*, the lattice of the surface clathrate atoms is *not* bipartite and energy optimization requires systematic search over the catalog of adatomic candidate sites. Our DFT-optimized catalog of added reconstruction sites is shown in Fig. 8, with site’s projected positions indicated by red open circles. These sites always reside about 3.4 Å *below* a 3-coordinated atom protruding outward from the surface layer, and they fall into four classes:

(1) Below the center of protruding pentagonal cap, for all  $c$ -subscripted T and R tiles. The sites appear *inside* the closed dodecahedron cage at the surface.

(2) Near the center of the *primed* T tiles. These sites occur inside largest, 28-atom cage, and in the case of  $T'_c$  triangle that has three nearby 3-coordinated neighbors, they are most reminiscent of the diamond-structure surface dumbbell configuration.

(3) Pairs of sites inside the R tiles.

(4) “Mid-edge” sites in  $R_h$  and  $T_h$ .

The surface energy calculation formally attributes increased energy relative to the bulk to the area of the open surface:

$$\Gamma = (E_{\text{cell}} - N_{\text{cell}}E_{\text{bulk}})/A, \quad (1)$$

TABLE II. Eight surface energies ( $\gamma_j^{\text{tile}}$  in  $\text{meV}/\text{\AA}^2$ ) for each kind of reconstructed tile in Fig. 8, fitted to Eq. (2).

$T_h$	$R_h$	$T'_h$	$R'_h$	$T_c$	$R_c$	$T'_c$	$R'_c$
23.1	23.3	22.4	22.5	23.3	22.2	26.4	25.9

where  $E_{\text{cell}}$  is energy per periodic cell,  $N_{\text{cell}}$  is the number of atoms within the cell,  $E_{\text{bulk}}$  is the energy per atom of the bulk structure, and  $A$  is the surface area of the cell.

However, surface energies of the tile terminations in Fig. 8 cannot be computed directly since even pure tilings of R or T tiles necessarily combine at least two types of the tiles, while the sample gives us single energy. Also, in order to weaken bias from having just one particular way of joining tiles together, more alternative tile-tile arrangements are necessary. In Table II, we report surface energies  $\gamma_j^{\text{tile}}$  [defined by Eq. (1)] of eight pure decagonal tiles (shown in Fig. 8), resulting from least-squares fit according to Eq. (2) for a collection of 15 slab samples labeled by  $i$ :

$$\Gamma_i = \sum_{j=1}^8 f_{ij} \gamma_j^{\text{tile}}, \quad f_{ij} = \frac{N_{ij} s_j}{A_i},$$

$$i \in \{1, \dots, 15\}, \quad j \in \{1, \dots, 8\} \quad (2)$$

where  $\Gamma_i$  is the surface energy of  $i$ th tile combination,  $f_{ij}$  is the fraction of  $i$ th sample surface  $A_i$  occupied by  $j$ th pure tile. More precisely,  $N_{ij}$  is the count of tile  $j$  in sample  $i$ , its area  $s_j$ 's are either  $S_R$  for R tile or  $S_T$  for T tile (see Sec. III C 1 for definition); and  $\gamma_j^{\text{tile}}$  are the eight fitted parameters: tile surface energies. The samples are based on three independent tilings, pure R, pure T, and  $R_2T_4$ . The terminations based on the latter tilings are discussed in detail below. Unit cells of the pure tilings must include pairs of tiles (see edge-matching rules in Fig. 8):  $R'_\alpha R_\alpha$  or  $T'_\alpha T_\alpha$ , where  $\alpha$  stands for “c”

or “h” vertex-column terminations. Bulk energies entering Eq. (1) are +28.8, +45.6, and +42.9  $\text{meV}/\text{atom}$  for T, R, and  $R_2T_4$  tilings, respectively, relative to bulk energy of  $\alpha$ -Sn (for comparison, in our DFT setup tetragonal  $\beta$ -Sn is +45.7  $\text{meV}/\text{atom}$ ). The samples, slabs and bulk, were relaxed until forces did not exceed 0.05  $\text{eV}/\text{\AA}$ . The “measured” surface energies  $\Gamma$  ranged between 22–25.5  $\text{meV}/\text{\AA}^2$ . The fitted surface energies  $\gamma^{\text{tile}}$  are nearly similar around 23  $\text{meV}/\text{\AA}^2$ , with the exception of  $T'_c$  and  $R'_c$  with  $\gamma_7^{\text{tile}} \sim \gamma_8^{\text{tile}} \sim 26 \text{ meV}/\text{\AA}^2$ . The standard deviation is 0.4  $\text{meV}/\text{\AA}^2$ , and maximal data-fit discrepancy is 0.65 in the same units. The range of the surface energies is comparable to that of hexagonal  $\gamma$ -Sn surfaces reported in Table II of Ref. [81]:  $\approx 21$ –28  $\text{meV}/\text{\AA}^2$ , and appreciably less than the  $\alpha$ -Sn (111)-type surface in  $(\sqrt{3} \times \sqrt{3})$ -type adatomic reconstruction (33  $\text{meV}/\text{\AA}^2$ ).

The relaxed configurations of all possible surface terminations of the  $R_2T_4$  approximant mixing together R and T tiles are shown in Figs. 10 and 11. The bulk  $R_2T_4$  structure is shown in Fig. S8 of SM [67] (VASP CONTCAR file is included in the SM named as “CONTCAR1” [67]). It has a space group  $Pbam$  (55) with 148 atoms in the unit cell. The optimized lattice parameters are  $a_{\text{ortho}} = 2.398 \text{ nm}$ ,  $b_{\text{ortho}} = 2.055 \text{ nm}$ , and  $c_{\text{ortho}} = 1.244 \text{ nm}$ ,  $c_{\text{ortho}}$  being the stacking direction. The surface terminations as defined in Fig. 8 combine two properties: “penta-cap” or “-hole” termination of the vertex column of dodecahedra, and primed (nonprimed) tile flavor [pink (light blue) colors]. From the edge-marking rules (green symbols in Fig. 8), all surface tiles in  $R_2T_4$  tiling must have the same coloring: this is a nongeneric property of a small periodic approximant (see representative example of large tiling from Fig. 7 in which pink and blueish tiles mix in a single layer). This leaves us with four terminations, that we implemented in three slab structures: both “penta-cap” terminations in Fig. 10 are bottom and top surfaces of the same 262-atom slab [made of  $(4F+3P)$ -type layers]. The primed “penta-hole” termination occurring on both surfaces of a 292-atom slab symmetrically are made of  $(3F+4P)$ -type layers (Fig. 11

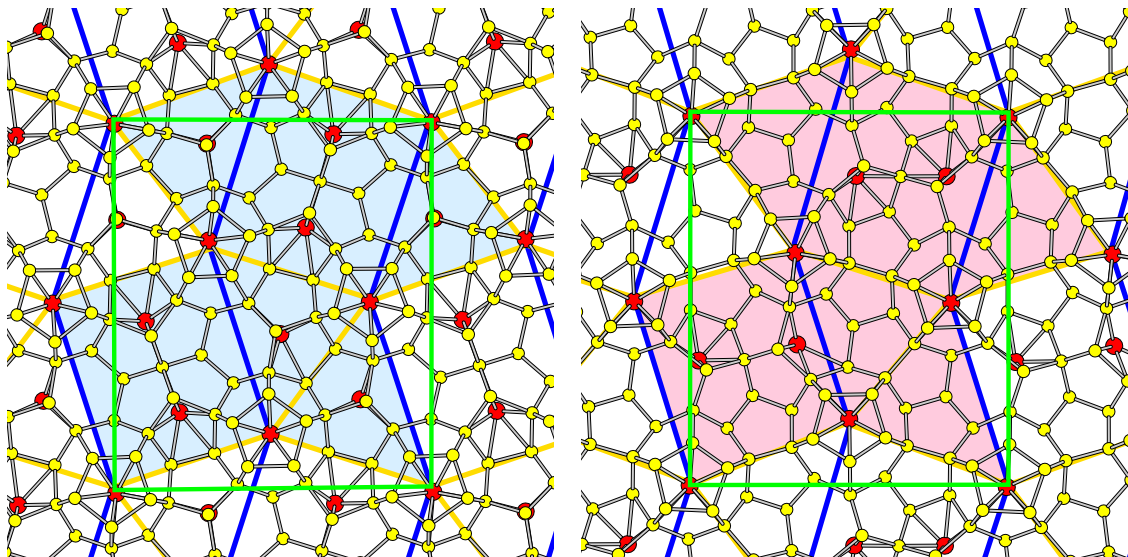


FIG. 10.  $4T'_c + 2R'_c$  (left) and  $4T_c + R_c$  (right) terminations of the  $R_2T_4$  clathrate structure. Adatoms are shown by red circles, a green rectangle outlines the periodic boundary in the  $ab$  plane.

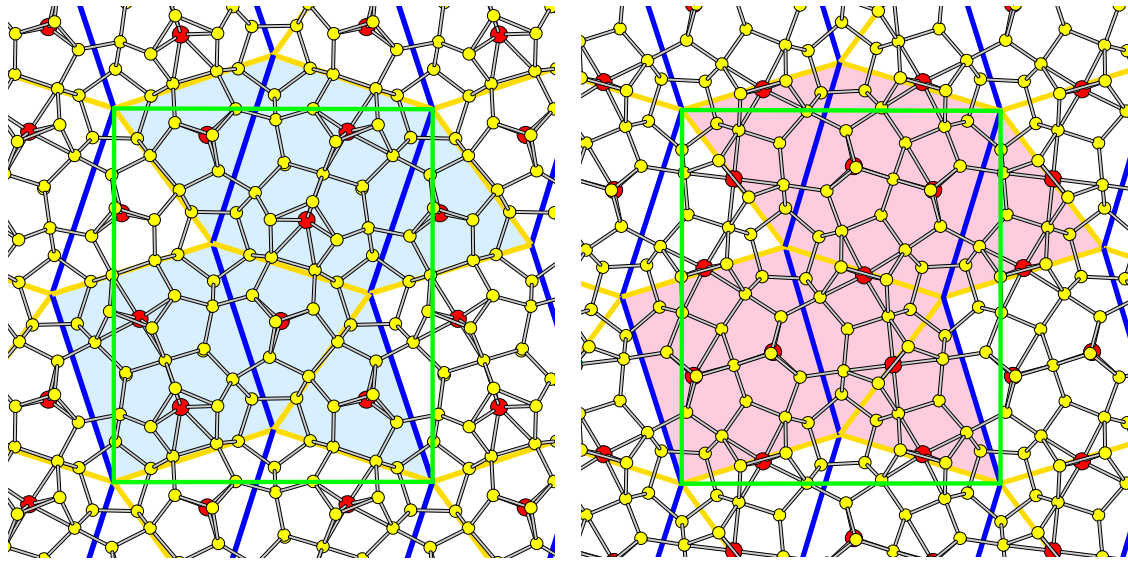


FIG. 11.  $4T'_h + 2R'_h$  (left) and  $4T_h + 2R_h$  (right) terminations of the  $R_2T_4$  clathrate structure. Adatoms are shown by red circles, a green rectangle outlines the periodic boundary in the  $ab$  plane.

left, blue tiling), and finally the nonprimed “penta-hole” reconstruction terminates a thinner ( $2F+3P$ , 220 atoms) slab structure (Fig. 11 right, pink tiling). It may be noted that each of the four surfaces of the  $R_2T_4$  approximant in Figs. 10 and 11 can be combined with numerical results from Table II following R/T labels given in the figure captions: the surface in Fig. 10 (left) has  $\gamma = 26 \text{ meV}/\text{\AA}^2$ , and all of the three other surfaces have  $\gamma = 22\text{--}23 \text{ meV}/\text{\AA}^2$ .

Our final remark is that the  $R_2T_4$  tiling nearly exactly matches the lattice parameters and atomic motifs in W-Al-Ni-Co approximant, serving as an important hint for nucleation of the decagonal clathrate on  $d$ -Al-Ni-Co, as discussed in Sec. III D. Combining  $\rho_\alpha$  for R and T tiles from Table I with  $R_2T_4$  tile counts and areas, we obtain coverings of  $\sim 0.4ML_\alpha$  for  $F$ -type layer and 1.09 for  $P$ -type layer. Figure 12(b) shows that the initial stage of the decagonal clathrate formation is  $F$ -type layer.

#### D. Nucleation of Sn on $d$ -Al-Ni-Co

Here, we focus on the question of how the decagonal Sn clathrate nucleates on the 10f  $d$ -Al-Ni-Co surface. As mentioned earlier, the bulk structure of  $d$ -Al-Ni-Co has been described by a decagonal W-Al-Ni-Co approximant phase that can be cleaved at the flat  $A$  surface or at the puckered  $B$  surface [54,55]. So, it can be expected that the local arrangement of atoms on the  $d$ -Al-Ni-Co surface is similar to that in W-Al-Ni-Co. We discuss henceforth the nucleation sites of Sn on W-Al-Ni-Co, and how that is compatible with formation of the Sn clathrate layer. The arrangement of Ni and Co, i.e., the transition metal (TM) atoms on the  $B$  surface of W-Al-Ni-Co [see Fig. 1(b) of Ref. [55]] can be described by the  $P1$  tiling. On the Al-Ni-Co surface, the adsorbed Sn atoms prefer to bind with the TM atoms. The preferential adsorption of Sn atoms around surface TM atoms with formation of Sn white flowers (SnWFs) at the early stages of the Sn deposition has been observed on  $i$ -Al-Pd-Mn [50].

On the  $B$  surface, there are two kinds of the preferred adsorption sites for Sn atoms. The first one is similar as that on the  $i$ -Al-Pd-Mn surface. The Sn atoms can be adsorbed around the TM atom centering a pentagon of Al atoms. The second kind is a small pentagon of TM atoms, where the Sn atoms are adsorbed in their bridge positions, compared to the clean  $B$  surface [see Fig. 1(b) of Ref. [55]]. Sn atoms can be adsorbed in the vertices of the  $P1$  tiling and together with the small Sn pentagon in the center they could create the SnWF configuration [Fig. 12(a)], which is similar as on the  $i$ -Al-Pd-Mn surface. On the other hand, Fig. 12(b) shows that on the  $B$  surface, small Sn pentagons can be adsorbed at the centers of the pentagons of the  $P1$  tiling (black lines). These pentagons can play the role of nucleation centers for growth of the Sn clathrate layer. The pentagon of Sn atoms can be adsorbed also in bridge positions of small Al pentagons (e.g., in the center of the figure) but such adsorption site is not preferred and not so stable as at the TM atoms.

If the surface in the center of the  $P1$  pentagon is occupied by a slightly protruding Co atom [right in Fig. 12(b)], the small  $Sn_5$  cluster (traced by red down pentagon) formed around this central atom is stable. The calculated average binding energy ( $E_b$ ) of Sn adatoms is  $E_b(Sn_5) = -0.501 \text{ eV/atom}$ . If the center of the  $P1$  pentagon is occupied by Al atoms [in the center of Fig. 12(b)] the position of the  $Sn_5$  adatoms (traced by dashed red up pentagon) is metastable with  $E_b(Sn_5) = -0.277 \text{ eV/atom}$ . However, it was observed that in this case the outer Sn atoms, which occupy the vertices of the  $P1$  pentagons [marked by a red circle in Fig. 12(a)] can significantly stabilize the central  $Sn_5$  cluster. Binding of outer 5 Sn atoms with the central  $Sn_5$  cluster forms the white flower (WF) configuration of 10 atoms (known also as the starfish cluster [82]). The WF configurations are frequently observed at deposition of adatoms on quasicrystalline surfaces [82–84]. The calculated binding energy of the WF cluster around the metastable  $Sn_5$  is  $E_b(Sn_{10}) = -0.396 \text{ eV/atom}$ . The WF cluster around the most stable  $Sn_5$  cluster [right in Fig. 12(b)] reduces the average binding energy to  $E_b(Sn_{10}) =$

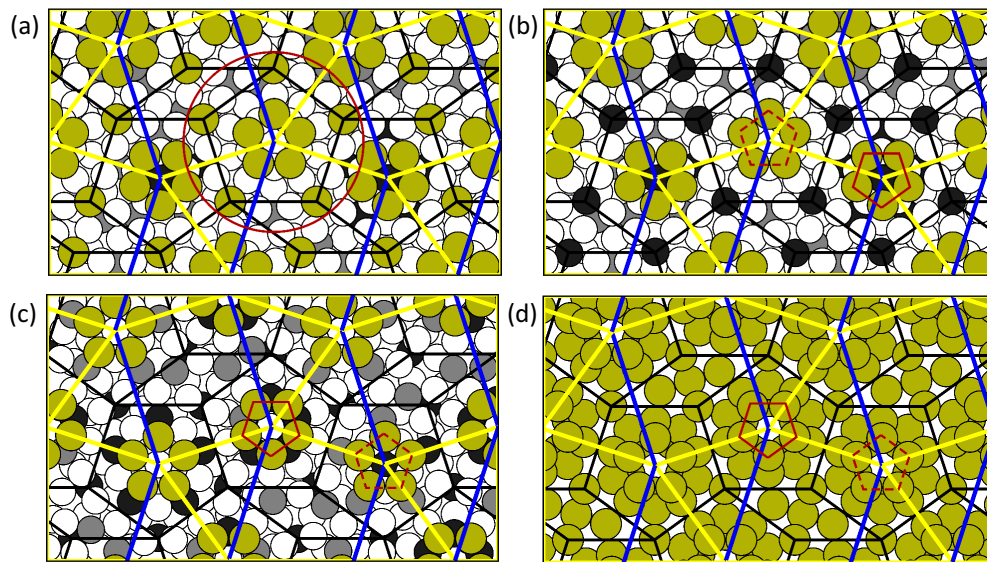


FIG. 12. Nucleation of Sn on the  $d$ -Al-Ni-Co surface represented by decagonal W-Al-Ni-Co approximant. Here, Al atoms are represented by open circles (Co by black, Ni by gray, and Sn atoms by dark yellow filled circles): (a) Sn white flower (enclosed by a red circle) on the  $B$  surface of the W phase. Sn pentagonal arrangement (solid and dashed red pentagons) on the (b)  $B$  surface and (c)  $A$  surface. (d) The atomic structure of the quasiperiodic Sn clathrate. The configuration of the Sn pentagon (dashed and solid red pentagon) is a part of the clathrate structure. Tilings are indicated by lines as Penrose (black) and rectangle triangle (R-T) tiling (blue and yellow).

$-0.426$  eV/atom. The WF configurations help to create the  $\text{Sn}_5$  clusters in the centers of the  $P1$  tiles and can thus support the nucleation and further growth of the clathrate structure.

On the  $A$  surface of W-Al-Ni-Co, the R-T tiling can also describe ordering of atoms on a larger scale but the local arrangement of atoms inside the tiles is less regular. Although the description of arrangement of the TM atoms on the  $A$  surface is described by its own tiling, and for the current discussion it is better to put on the  $A$  surface together with the R-T tiling also the same  $P1$  tiling as on the  $B$  surface. On the  $A$  surface, there is a higher content of TM atoms compared to the  $B$  surface. Similarly as on the  $B$  surface, they can form small TM pentagons (e.g., in the center of the figure) [Fig. 12(c)]. These small TM pentagons can be preferred adsorption centers for the Sn atoms adsorbed in the bridge positions between the TM atoms. Figure 12(c) shows the  $A$  surface with the Sn pentagons in vertices of the R-T tiling. Similarly as on the  $B$  surface, these can be the possible nucleation centers for growth of the clathrate layer on the  $A$  surface. However, on this surface there are also additional TM atoms (inside the thin rhombi of  $P1$ ) which can disturb the presented regular ordering of the Sn nucleation centers.

Figure 12(d) shows the Sn clathrate layer that is described by the R-T tiling model (thick blue and yellow lines). The orientation of the Sn pentagons alternates with the number of the Sn clathrate layers. The present one is for one or odd number of layers. Further, on the  $B$  surface of the W phase, the length of the Penrose  $P1$  tiling is  $d(P1) = 0.758$  nm [55]. From this it follows that the lengths of the blue and yellow edges of the R-T tiling (Fig. 12) are  $d(\text{blue}) = \tau \times d(P1) = 1.227$  and  $d(\text{yellow}) = d(\text{blue})/[2 \times \sin(\pi/5)] = 0.851 \times d(\text{blue}) = 1.043$  nm, respectively. The length of edges of the R-T tiling on the  $d$ -Al-Ni-Co surface is thus 2.1% smaller compared to the  $i$ -Al-Pd-Mn surface [50], indicating that they are almost the same. The sizes of the R-T tilings on the W phase and

$d$ -Al-Ni-Co are likely to be within 1%–2%. It is remarkable that the lengths of the R-T edges for W-Al-Ni-Co surface [ $d(\text{yellow}) = 1.043$  nm and  $d(\text{blue}) = 1.227$  nm] are so close to those of the decagonal Sn clathrate obtained from DFT in Sec. III C 1 ( $a = 1.082$  nm and  $b = 1.268$  nm) (see also Ref. [85]).

To check the compatibility of the SnWF and the pentagon with the clathrate structure, it is important to compare the configuration of Sn adatoms forming the SnWF cluster and the pentagon on the  $A$  and  $B$  surfaces of W-Al-Ni-Co [Figs. 12(a)–12(c)] with the structure of the clathrate layer [Fig. 12(d)]. The clathrate structure consists of regular dodecahedral cages of Sn atoms. The dodecahedra are centered at the vertices of the rectangular-triangular (R-T) tiling. It is clear from Fig. 12 that SnWF and the pentagons are the integral parts of the clathrate surface.

In order to experimentally probe the nucleation of the Sn clathrate on  $d$ -Al-Ni-Co, we have performed STM after 0.2 ML Sn deposition (Fig. 13). A large part of the image is dispersed with isolated Sn atoms that have an atomic height of  $0.17 \pm 0.02$  nm after averaging over 110 height profiles over different Sn adatoms. However, in some regions nucleation of Sn pentagons is clearly observed as highlighted by dashed red circles in Fig. 13(a). The average diameter of the dashed red circles that enclose these pentagons is  $1.5 \pm 0.1$  nm. Furthermore, a SnWF of about 2 nm diameter [yellow circle in Figs. 13(a) and 13(b)] is also observed, as discussed above for the W-Al-Ni-Co  $B$  surface [red circle in Fig. 12(a)]. In Fig. 13(c), two pentagons that are  $36^\circ$  rotated with respect to each other are traced by dashed red and black pentagons, respectively. It may be noted that such rotated pentagonal motifs are also expected from our nucleation model discussed above for both  $B$  and  $A$  surfaces [dashed and solid red pentagons in Figs. 12(b) and 12(c)]. Figure 13(d) shows how a pentagonal motif converts to a SnWF with Sn atoms bonding

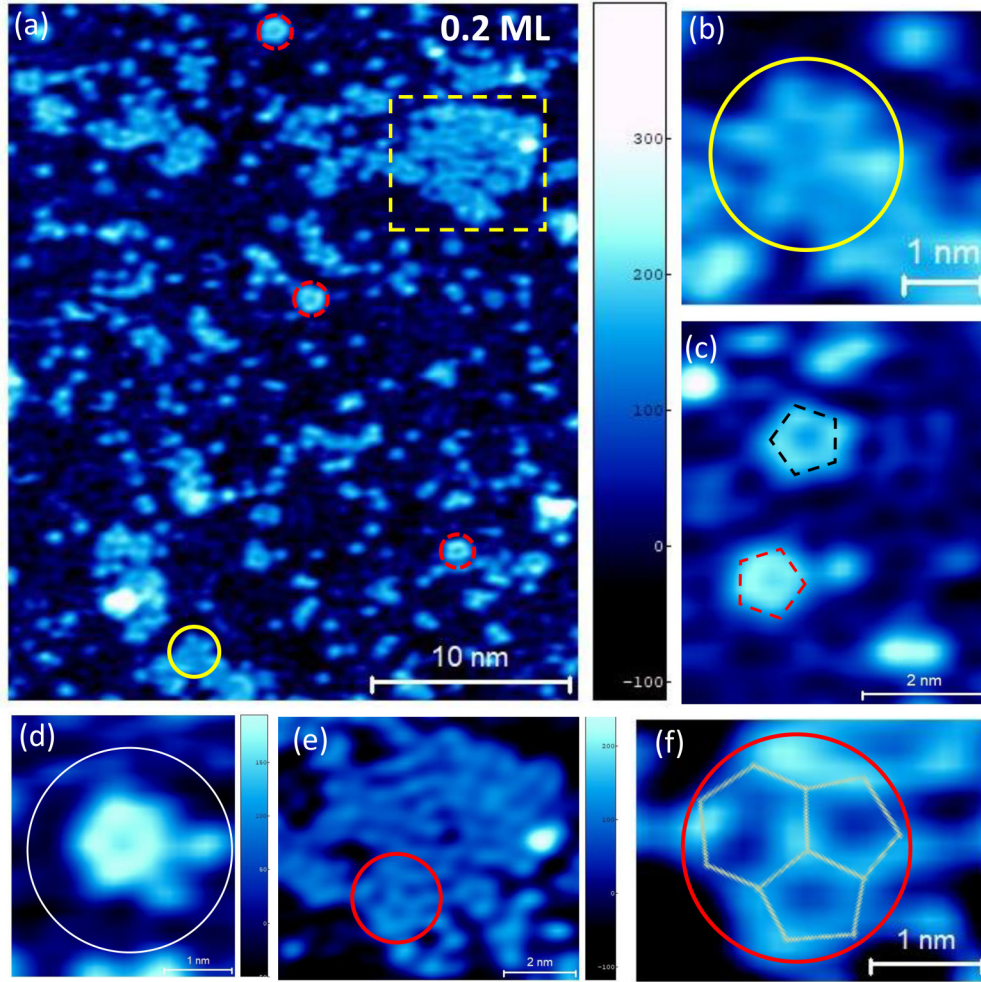


FIG. 13. (a) STM topography image of 0.2 ML Sn/ $d$ -Al-Ni-Co with  $I_T = 0.5$  nA,  $U_T = -1.5$  V. Sn white flower [yellow circle, zoomed in (b)] and pentagonal motifs (dashed red circle). (c) Two pentagonal motifs (traced by dashed red and black lines) are rotated by  $36^\circ$  with respect to each other. (d) Sn atoms attached to the pentagonal motifs. (e) The region inside the dashed yellow rectangle in (a) shown in an expanded scale. A triplet motif comprising of two pentagons and a hexagon (red circle) is zoomed and compared with the  $R_2T_4$  model in (f).

at its vertices. A region where Sn motifs coalesce to form an island [dashed yellow rectangle in Fig. 13(a)] is shown in an expanded scale in Fig. 13(e). Here, motif (red circle) formed by two pentagons and a hexagon is visible, shown zoomed Fig. 13(f). This, named as triplet motif, is compared with and shown to be a valid part of both penta-cap and penta-hole terminations of the  $R_2T_4$  approximant in Fig. 15. Thus, the indication of formation of the clathrate structure is obtained even from small Sn islands at initial stage of the growth.

#### E. $R_2T_4$ approximant model of the Sn film on Al-Ni-Co substrate

The W-phase approximant model structure [54] with its 530 atoms/cell utilized as a model substrate for nucleation in Sec. III C strains the resources when the computationally intensive *ab initio* approach is needed. At the same time, the W-phase periodic cell is *double superstructure* of the  $R_2T_4$  approximant cell (the horizontal axis of the W-phase periodic cell in Fig. 12 is doubled along the horizontal axis relative to the  $R_2T_4$  cell in Figs. 10 and 11). So, possibly a hypothetical  $R_2T_4$  Al-Ni-Co approximant preserves equally fair

relationship with the  $d$  phase while requiring only  $\sim 10\%$  of the resources needed to study composite Sn/Al-Ni-Co slab within our DFT setup. The  $R_2T_4$  Al-Ni-Co should not be confused with the  $R_2T_4$  clathrate approximant because although they share the tiling geometry, the atomic motifs behind this coincidence are very different.

We carried out tempering simulations for the Al-Ni-Co system in the  $R_2T_4$  cell in the spirit of the Al-Cu-Fe simulated annealing leading to spontaneous formation of icosahedral quasicrystal [86], using DFT-fitted empirical oscillating potentials (EOP) [87] for Al-Ni-Co. Figure 14(a) displays  $R_2T_4$ -Al-Ni-Co bilayer at the  $B$ -type surface analogous to its W-phase counterpart in Fig. 12(b). Details of the preparation of the  $R_2T_4$ -Al-Ni-Co model are gathered as a note in the SM [67], and the final DFT-relaxed structure is provided in the SM as “CONTCAR2” [67].

Although atomic structure of  $d$ -Al-Ni-Co and Sn clathrate obey completely different electronic and coordination rules, their interface is perfectly coherent following the R-T tiling geometry, as indicated in Fig. 12. This allows for a straightforward approach to the Sn/Al-Ni-Co  $R_2T_4$  approximant composite model construction: we merge a three-layer thick

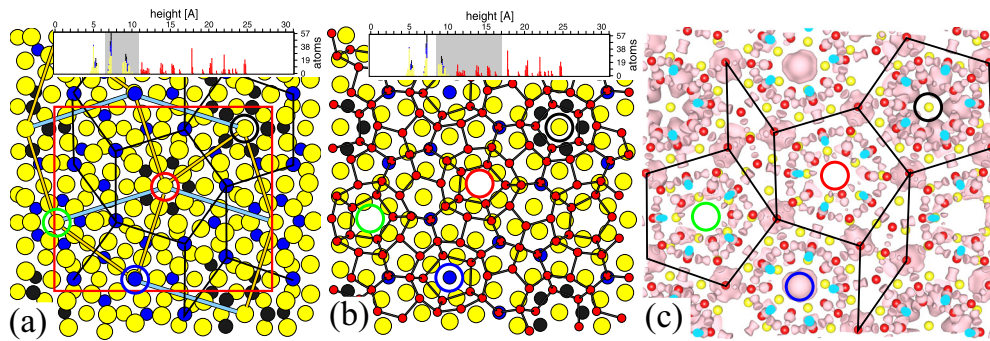


FIG. 14.  $R_2T_4$  approximant Sn/Al-Ni-Co slab structure after DFT relaxation: (a) Al-Ni-Co “top” bilayer near the interface; (b) slice including “topmost” Al-Ni-Co layer with “bottom”  $FP$  layers of the Sn film. Height histograms inserted at the top of panels indicate displayed slice selection by grayed background. Atoms are represented by colored circles: Al (yellow), Co (blue), Ni (black), Sn (red), the same for histogram bars representing counts of the atoms. (c) Pink isosurfaces of the valence charge density for the slice shown in (b). Cyan areas indicate section opening view *inside* the isosurface.

Al-Ni-Co slab (two Al-rich “puckered” layers with “flat” pseudomirror layer in-between) with a five-layer 1.2 nm-thick Sn slab (three  $F$ -type and two  $P$ -type layers). The slabs were positioned within plausible distance from each other, with shortest initial pair distances of  $\sim 0.27$  nm between Sn and Al/Co/Ni atoms. The open-surface side of the Sn slab was reconstructed following the primed-penta-cap recipe illustrated in Fig. 10 left, and 1.2 nm-thick vacuum slab was inserted between the Sn surface and the “bottom” of the periodic image of Al-Ni-Co slab. The resulting composite slab had  $\text{Sn}_{180}/\text{Al}_{150}\text{Co}_{32}\text{Ni}_{18}$  content in the  $a_s = 2.34$  nm,  $b_s = 1.98$  nm, and  $c_s = 3.09$  nm orthorhombic cell (the  $c_s$  axis is parallel to the pseudo-10f axis), and its “bottom”  $PF$  layers relaxed structure is presented in Fig. 14(b). The final optimized structure can be found in “CONTCAR3” [67].

The structural relaxation was executed under our DFT setup, using 4 and finally 16  $k$ -points mesh, but with the rectangular cell fixed at bulk Al-Ni-Co- $R_2T_4$  optimal  $a_s \times b_s$  size. During the relaxation, the structure settled quickly into a local minimum with negligible residual forces and rather small  $-3$  kBar pressure. In order to estimate strength of the binding between Sn/Al-Ni-Co slabs, we separated Sn and Al-Ni-Co sublabs by another 1.2 nm-wide vacuum gap, and re-relaxed the structure (holding the cell fixed). We find the “work of separation” (or *adhesion*) defined as  $W_{\text{sep}} = \Delta E/A \sim 60.4$  meV/Å<sup>2</sup> (area  $A = a_s b_s$  and  $\Delta E$  is the energy of the composite slab deducted by the energies of the vacuum-separated Sn and Al-Ni-Co slabs in eV *per cell*) to be nearly identical to the  $W_{\text{sep}} \sim 64.4$  meV/Å<sup>2</sup> of the pure clathrate II structure normal to its threefold cubic direction. This shows that the strength of the attachment between the Sn-clathrate film and the Al-Ni-Co substrate is close to the self-separation of the clathrate itself.

The gross picture offered by charge-density isosurface taken at  $\rho_{\text{el}}/\rho_{\text{el}}^{\text{max}} = 0.02$  ( $\rho_{\text{el}}$  denotes the valence electron density) and displayed in Fig. 14(c) [slice widths as Fig. 14(b)] is as follows: the charge mainly accumulates around transition metal (TM) atoms (that are hidden inside the isosurfaces), with lobes of the surfaces pointing toward the Al or Sn atoms, and indicating a charge transfer from the Al/Sn atoms. Second, with the exception of the “bottom-most” Sn atoms, characteristic dumbbell-like charge pockets

accumulate around the Sn-Sn bond midpoints, indicating clear  $sp^3$  character of these electronic states. Side view of the isosurfaces (not shown) reveals that the crucial interface bonding occurs via strong covalent 0.27 nm bonds normal to the interface between Sn and Co atoms, located at the vertices of the  $P1$  tiling [black lines Fig. 14(c)]: these are the well-known  $WF$ -cluster tips introduced in the previous section.

To summarize, DFT study of the Sn/Al-Ni-Co interface based on the  $R_2T_4$  tiling geometry confirms that (i) there are essentially two types of Sn atoms in the first ML: isolated Sn at the vertices of the  $P1$  tiling above Co atoms bonding to them by strong covalent bonds; and Sn pentagons at the vertices of the R-T tiling, occurring above several distinct pentagonal Al-Ni-Co motifs, supporting the findings of the previous section; (ii) above this first ML, Sn builds up stable  $sp^3$ -bonded clathrate structure.

#### F. Motifs from STM compared to the relaxed $R_2T_4$ structural model

In this section, we define the different types of motifs, each highlighted by similar line type in the STM images in Figs. 1, 3, 4, and 13 based on the energy-optimized relaxed surface of the  $R_2T_4$  clathrate approximant in Fig. 15. Thereafter, a comparison is provided between STM and theory in Figs. 16 and 17.

The *wheel* motif enclosed by dashed orange circle in Fig. 15 is a nearly decagonal congregation of 10 polygons (8 pentagons and 2 hexagons) with common sides. Sn atoms decorate their vertices. Incomplete wheels with more than five polygons are also referred to as the wheel motif. Also note that the polygons are not regular, the lengths of their sides have a mean value of 0.3 nm with standard deviation of  $\pm 0.01$  nm (Fig. 15). A perfectly decagonal wheel with 10 pentagons does not occur in the  $R_2T_4$  approximant, but this is a feasible object if a bigger approximant is considered. It simply corresponds to a particular tiling pattern, namely, five triangles forming pentagons with blue tiling edges. The wheel motifs are found on both the “penta-cap” and “penta-hole” surfaces, as shown in Figs. 15(a) and 15(b), respectively. In the former, the decagon is capped with the possible occurrence



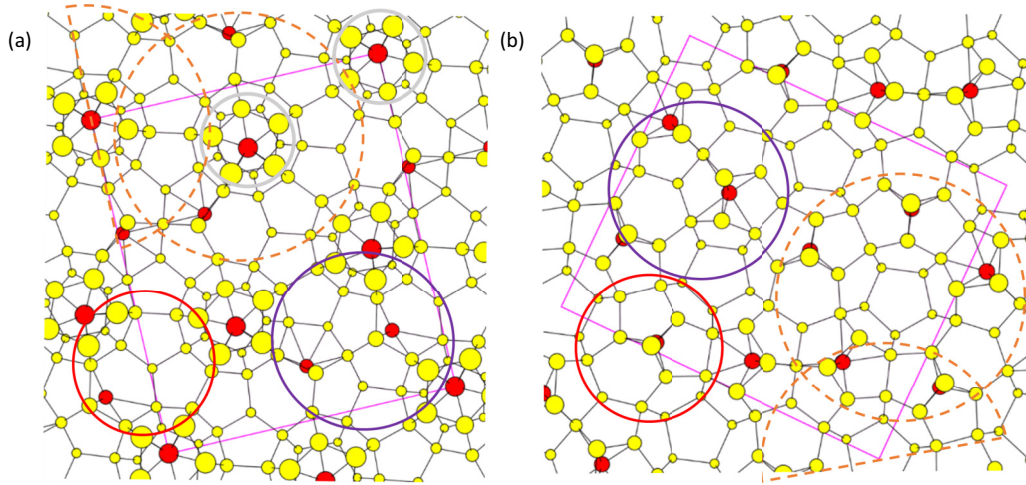


FIG. 15. Energy-optimized relaxed surface of the  $R_2T_4$  clathrate approximant with (a) “penta-caps” reconstruction and (b) “penta-hole” reconstruction, the pink rectangle shows the unit cell. The motifs are highlighted by circles: wheel (dashed orange), polygon assembly (violet), triplet (red), pentagon (gray), and crown (dashed orange half-circle). The sizes of the yellow filled circles representing the Sn atoms scale with their vertical height, red filled circles mark the Sn adatom positions.

of adatom, which would give a bright contrast at the center in the STM image. In the latter, the decagon is not capped, resulting in a relatively darker center of the wheel motif. The *crown* motif is a part of the wheel motif comprising of  $\leq 5$  polygons highlighted by a dashed orange half-circle in Fig. 15. The *polygon assembly* with variable number of polygons comprises of the overlapping regions of two adjacent wheel motifs and consists of pentagons with and without a hexagon (violet circles). The *triplet* motif is a smaller version of the polygon assembly, comprising of two pentagons and one hexagon (red circles). The *pentagon* motif has its vertices decorated by the five topmost Sn atoms in the center region of the “penta-cap” wheel, as shown by a gray circle in Fig. 15(a).

The above defined motifs are compared with the STM images in Fig. 16 for two different thicknesses. It is interesting to observe that there is an inflation between the motifs of the monolayer [Figs. 16(a)–(16e)] and the 10 nm film [Figs. 16(f)–(16j)], which is estimated to be  $\sim \tau^2 \chi$ . For example, the average diameter of the wheel motif is  $4.5 \pm 0.5$  nm for monolayer,  $8.8 \pm 1$  nm for 0.9 nm, and  $14.5 \pm 1$  nm for the 10 nm film. This shows inflation by a factor of  $3.2 \pm 0.4$  between monolayer and the 10 nm film, which is close to  $\tau^2 \chi$  ( $= 3.08$ ). Similarly, inflation by a factor of  $1.65 \pm 0.2$  between the 0.9 and the 10 nm films is close to  $\tau$  ( $= 1.618$ ). This is consistent with the finding that the theoretical model requires an inflation of  $\tau^2$  for good agreement with the sizes of the monolayer motifs, whereas it is  $\tau^3 \chi$  for the 0.9 nm film and  $\tau^4 \chi$  for the 10 nm film.

Inflation is a well-known property of the quasiperiodic systems due to their self-similar nature and has been observed in both ternary and binary quasicrystals [50,89–92]. A well-known example is *i*-Al-Pd-Mn, where the fundamental intercluster linkage of  $7.75 \text{ \AA}$  is  $\tau$  ( $\tau^3$ ) inflated along the twofold (fivefold) direction.  $\tau^3$  inflation has also been reported in a binary quasicrystal Yb-Cd with the formation of a cluster of clusters [90]. Inflation could be caused with respect to the theoretical model by the formation of self-similar

structures with the inclusion of extra atoms such that the local bonding characteristics remain similar. In our previous work, we showed that the STM image from (3–4) nm-thick Sn film on *i*-Al-Pd-Mn shows  $\tau^3$  inflation with respect to the theoretical clathrate model [50]. Here, from Fig. 16, we find satisfactory agreement in the sizes of the STM motifs and the  $R_2T_4$  model at a fixed inflated length scale for all the motifs at a particular thickness. This is an indication of the propagation of quasiperiodic ordering in the film.

The pentagon motif in Figs. 16(a) and 16(f) is the smallest of all the motifs and is traced by black lines that join the bright vertices. It is also the most abundantly observed motif, for example, see Fig. 4(d). The tracing of the triplet motif by black lines revealing its internal structure is shown in Figs. 16(b) and 16(g). The tracings of these motifs are juxtaposed on the  $R_2T_4$  model below each image in the same length scale, and the agreement is rather good for both the thicknesses vindicating the clathrate model. Note that the triplet motif is also observed for 0.2 ML Sn deposition in Fig. 13(f), and the agreement with the  $R_2T_4$  model is satisfactory.

The polygon assembly motif is also observed in both the monolayer as well as the thick film, as shown in Figs. 16(c) and 16(h), respectively. The crown motif in Fig. 16(d) with bright center for the monolayer in contrast to a dark centered one in Fig. 16(g) for the 10 nm film shows existence of both “penta-cap” and “penta-hole” type surfaces. A crown motif on the 0.9 nm Sn film is shown in Fig. S6(a) of SM [67]. The wheel motifs are shown in Figs. 16(e) and 16(j), as well as in Figs. S4(b) and S6(b) of SM [67], the latter being for the 0.9 nm-thickness film. When juxtaposed on the  $R_2T_4$  model, the tracings of these bigger motifs (polygon assembly, crown, and wheel) reveal their size similarity after inflation. Moreover, the ratio of the sizes of the pentagon and the wheel motifs is in good agreement between STM and theoretical model. However, in contrast to smaller motifs such as the pentagon and triplet, the underlying structure of the larger motifs is only partially consistent with the clathrate model.

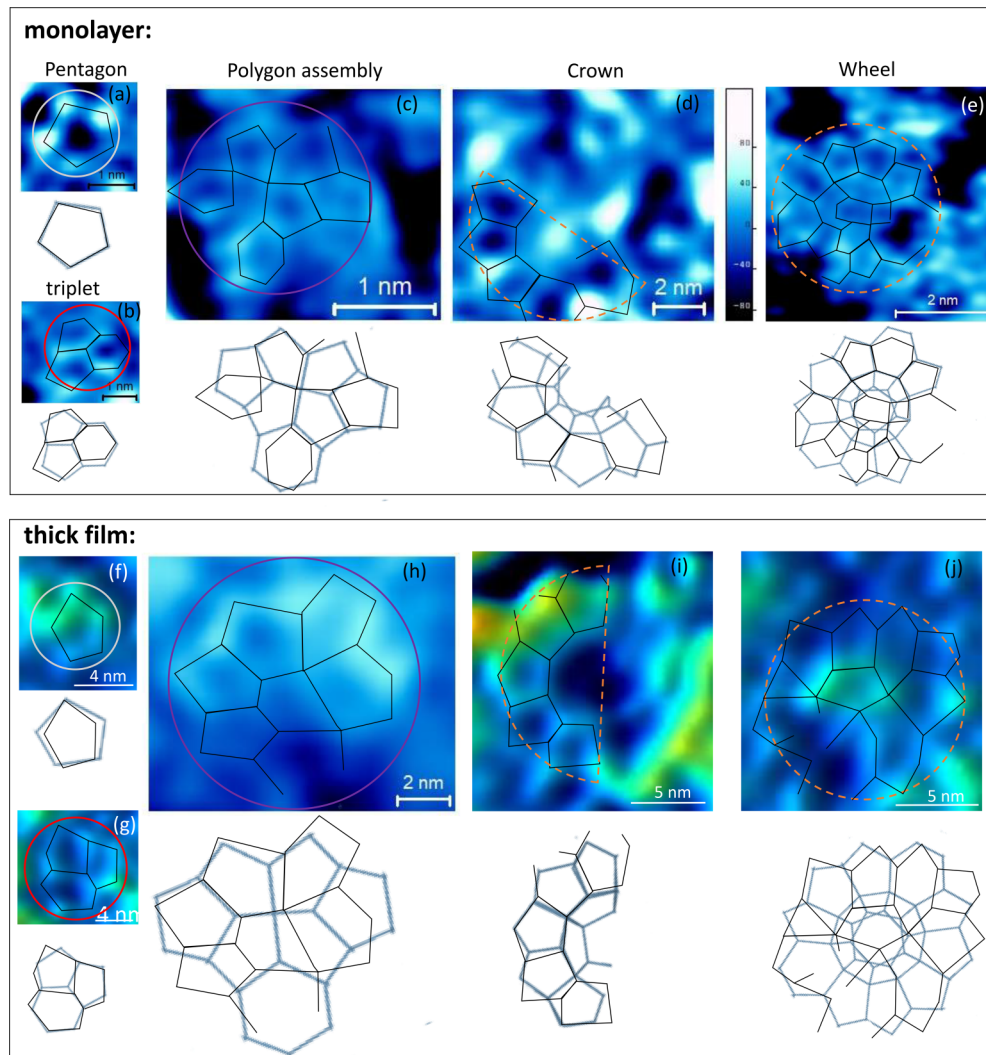


FIG. 16. The different types of motifs (indicated at the top of each figure column) such as pentagon (gray circle), triplet (red circle), polygon assembly (violet circle), crown (dashed orange half-circle), and wheel (dashed orange circle) observed from STM for (a)–(e) the monolayer and (f)–(j) the 10 nm-thick film. Each motif is traced by black lines [some untraced images are provided in Figs. S9(e)–S9(h) for comparison] and juxtaposed on the relaxed surface of the  $R_2T_4$  clathrate approximant (light blue lines) in the same scale below each STM image. The  $R_2T_4$  approximant was inflated by  $\tau^2$  and  $\tau^4\chi$  for the monolayer and the thick film, respectively.

Nevertheless, this partial agreement is also a significant result given that stochastic processes and competing disorder would have a greater influence on the bigger motifs. Moreover, the puckering and roughness of the films could also play a role. This is also revealed in the theoretical model, where the atoms deviate considerably from the  $x$ - $y$  plane: Fig. 15 shows that the average height of the Sn atoms is  $z = 0.25 \pm 0.12$  nm, where the standard deviation provides an estimate of the puckering. In the  $R_2T_4$  model, two Sn atoms, for instance, forming a side of the pentagon in the wheel motif and pointing in the radial direction, are often at a greater height than the remaining three atoms. In STM, this side would look brighter, but other sides containing Sn atoms at a lower height may appear darker. Thus, the STM pictures may not depict entire and regular polygons. The comparatively modest size of the  $R_2T_4$  approximant may also contribute to the discrepancy between STM and the model; the internal structure of a larger approximant may result in a better agreement.

In Fig. 17, the different motifs (numbered 1–9) of  $R_2T_4$  approximant clathrate model are overlaid on (white lines) the STM image of the Sn thick film after allowing for rotation (motifs 2–9 need to be rotated by different angles with respect to motif 1). In this way, we find that a region of  $800 \pm 50$  nm<sup>2</sup> is in good agreement with our model. Requirement of rotation can be related to the the formation of ring joining the spots in the LEED pattern [Figs. 5(a) and 5(b)]. The regions that do not follow the  $R_2T_4$  model are traced by black dashed lines in Fig. 17. Such regions could exist because of competing disordered structures since for the thick Sn films with clathrate multilayers (that has not been calculated by DFT), the advantage of interfacial compatibility would be reduced.

Last but not least, the Sn motifs on *i*-Al-Pd-Mn that reflect the clathrate structure [50] and those on *d*-Al-Ni-Co exhibit a considerable degree of similarity. Figure S9 [67] depicts this for the pentagon, triplet, crown, and wheel designs. The formation of the clathrate quasiperiodic structure on two distinct

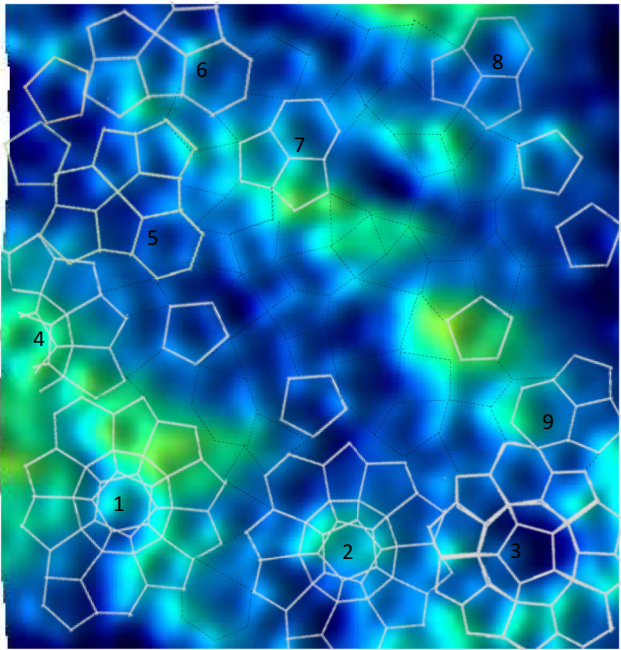


FIG. 17. A portion of the STM image of the 10 nm-thick Sn film [enclosed by white dashed rectangle in Fig. 4(d)] compared with motifs such as wheel (numbered as 1–3), crown (4), polygon assembly (5 and 6), and triplet (7–9) after inflation (white lines). The regions that are not in agreement with the  $R_2T_4$  approximant model are traced by black dashed lines.

types of quasicrystalline surfaces implies that it is an inherent characteristic of Sn.

#### IV. CONCLUSIONS

We have carried out a combined experimental and theoretical study to probe the possible occurrence of quasiperiodicity in Sn films grown on *d*-Al-Ni-Co up to an average thickness of 10 nm. Decagonal spots in the LEED pattern, characteristic motifs, and the FFT of the STM topography images establish decagonal quasiperiodicity in the Sn thin film ( $<1$  nm). For

the thicker films up to the largest thickness of 10 nm where the effective potential of the substrate is negligible [88,93], the motifs, weak LEED, and FFT are also observed, showing that partial decagonal structural correlations are maintained in spite of the competing disorder. The clathrate atomic positions of the DFT-relaxed decagonal clathrate structure reveal remarkable inflation relationship with STM. The internal structure of the smaller motifs such as pentagon and triplet show good agreement with our DFT-based relaxed  $R_2T_4$  approximant clathrate structural model, while for the larger motifs the agreement is partial. This model is the most-likely hypothesis for the Sn structure because (i) compatibility of the clathrate structure with the substrate resulting from very similar edge lengths (within 1%) of the R-T tiling of the  $R_2T_4$  approximant and the *B* surface of W-Al-Ni-Co approximant for the *d*-Al-Ni-Co surface, (ii) the ground states of the thicker slabs are  $sp^3$  bonded, the metallic Sn structures are only stabilized by vibrational entropy at elevated temperatures, (iii) the clathrate has significantly lower surface energy than the  $\alpha$ -Sn, hence, for sufficiently thin films clathrate structure has lower energy, and (iv) the “work of separation” or “adhesion” of Sn/*d*-Al-Ni-Co turns out to be comparable to the same quantity calculated for the clathrate itself proving that the clathrate Sn effectively binds to the *d*-Al-Ni-Co surface.

#### ACKNOWLEDGMENTS

M.M. and M.K. are thankful for the support from the Slovak Grant Agency VEGA (Grant No. 2/0144/21) and APVV (Grants No. 15-0621 and No. 19-0369). Parts of the calculations were performed in the Computing Center of the Slovak Academy of Sciences using the supercomputing infrastructure acquired under Projects No. ITMS 26230120002 and 26210120002. R. Batabyal is especially thanked for important suggestions and a careful reading of the manuscript. M. Balal, P. Sadhukhan, and S. Barman are thanked for support. The growth of *d*-Al-Ni-Co single grain substrate done at Ames laboratory was supported by the U.S. Department of Energy, Office of Basic Energy Science, Division of Materials Sciences and Engineering. Ames Laboratory is operated for the U.S. Department of Energy by Iowa State University under Contract No. DE-AC02-07CH11358.

- 
- [1] D. Shechtman, I. Blech, D. Gratias, and J. W. Cahn, *Phys. Rev. Lett.* **53**, 1951 (1984).
  - [2] A. P. Tsai, J. Q. Guo, E. Abe, H. Takakura, and T. J. Sato, *Nature (London)* **408**, 537 (2000).
  - [3] S. Fischer, A. Exner, K. Zielske, J. Perlich, S. Deloudi, W. Steurer, P. Lindner, and S. Förster, *Proc. Natl. Acad. Sci. USA* **108**, 1810 (2011).
  - [4] D. V. Talapin, V. E. Shevchenko, I. M. Bodnarchuk, X. Ye, J. Chen, and C. B. Murray, *Nature (London)* **461**, 964 (2009).
  - [5] C. Xiao, N. Fujita, K. Miyasaka, Y. Sakamoto, and O. Terasaki, *Nature (London)* **487**, 349 (2012).
  - [6] X. Ye, J. Chen, M. E. Irrgang, M. Engel, A. Dong, S. C. Glotzer, and C. B. Murray, *Nat. Mater.* **16**, 214 (2017).
  - [7] J. D. Cain, A. Azizi, M. Conrad, S. M. Griffin, and A. Zettl, *Proc. Natl. Acad. Sci. USA* **117**, 26135 (2020).
  - [8] S. J. Ahn, P. Moon, T.-H. Kim, H.-W. Kim, H.-C. Shin, E. H. Kim, H. W. Cha, S.-J. Kahng, P. Kim, M. Koshino, Y.-W. Son, C.-W. Yang, and J. R. Ahn, *Science* **361**, 782 (2018).
  - [9] W. Yao, E. Wang, C. Bao, Y. Zhang, K. Zhang, K. Bao, C. K. Chan, C. Chen, J. Avila, M. C. Asensio, J. Zhu, and S. Zhou, *Proc. Natl. Acad. Sci. USA* **115**, 6928 (2018).
  - [10] L. Bindi, J. M. Eiler, Y. Guan, L. S. Hollister, G. MacPherson, P. J. Steinhardt, and N. Yao, *Proc. Natl. Acad. Sci. USA* **109**, 1396 (2012).

- [11] S. S. Kang, J. M. Dubois, and J. V. Stebut, *J. Mater. Res.* **8**, 2471 (1993).
- [12] J. M. Dubois, S. S. Kaing, and A. Perrot, *Mater. Sci. Eng.: A* **179–180**, 122 (1994).
- [13] S. J. Poon, *Adv. Phys.* **41**, 303 (1992).
- [14] S. Sarkar, M. Krajić, P. Sadhukhan, V. K. Singh, A. Gloskovskii, P. Mandal, V. Fournée, M.-C. de Weerd, J. Ledieu, I. R. Fisher, and S. Roy Barman, *Phys. Rev. B* **103**, L241106 (2021).
- [15] J. Nayak, M. Maniraj, A. Rai, S. Singh, P. Rajput, A. Gloskovskii, J. Zegenhagen, D. L. Schlagel, T. A. Lograsso, K. Horn, and S. R. Barman, *Phys. Rev. Lett.* **109**, 216403 (2012).
- [16] R. Chen, C.-Z. Chen, J.-H. Gao, B. Zhou, and D.-H. Xu, *Phys. Rev. Lett.* **124**, 036803 (2020).
- [17] J. Fan and H. Huang, *Front. Phys.* **17**, 13203 (2022).
- [18] P. Guyot and M. Audier, *C. R. Phys.* **15**, 12 (2014).
- [19] F. C. Frank and J. S. Kasper, *Acta Crystallogr.* **11**, 184 (1958).
- [20] F. C. Frank and J. S. Kasper, *Acta Crystallogr.* **12**, 483 (1959).
- [21] D. R. Nelson and F. Spaepen, *Solid State Phys.* **42**, 1 (1989).
- [22] J.-F. Sadoc and R. Mossieri, *Geometric Frustration* (Cambridge University Press, Cambridge, 1999).
- [23] D. P. Shoemaker and C. B. Shoemaker, in *Introduction to Quasicrystals*, edited by M. V. Jaric (Academic, London, 1988), pp. 1–57.
- [24] V. Elser and C. L. Henley, *Phys. Rev. Lett.* **55**, 2883 (1985).
- [25] M. Audier and P. Guyot, *Philos. Mag. B* **53**, L43 (1986).
- [26] S. Sachdev and D. R. Nelson, *Phys. Rev. B* **32**, 4592 (1985).
- [27] M. C. Schäfer and S. Bobev, *J. Am. Chem. Soc.* **135**, 1696 (2013).
- [28] Y. Sun, J. Lv, Y. Xie, H. Liu, and Y. Ma, *Phys. Rev. Lett.* **123**, 097001 (2019).
- [29] H. Lin, S. Lee, L. Sun, M. Spellings, M. Engel, S. C. Glotzer, and C. A. Mirkin, *Science* **355**, 931 (2017).
- [30] L. Zhu, G. M. Borstad, H. Liu, P. A. Guńka, M. Guerette, J.-A. Dolyniuk, Y. Meng, E. Greenberg, V. B. Prakapenka, B. L. Chaloux, A. Epshteyn, R. E. Cohen, and T. A. Strobel, *Sci. Adv.* **6**, eaay8361 (2020).
- [31] M. S. Ikeda, H. Euchner, X. Yan, P. Toměš, A. Prokofiev, L. Prochaska, G. Lientschnig, R. Svagera, S. Hartmann, E. Gati, M. Lang, and S. Paschen, *Nat. Commun.* **10**, 887 (2019).
- [32] L. Zhu, T. A. Strobel, and R. E. Cohen, *Phys. Rev. Lett.* **125**, 127601 (2020).
- [33] J. Ghosh, R. R. J. Methikkalam, R. G. Bhui, G. Ragupathy, N. Choudhary, R. Kumar, and T. Pradeep, *Proc. Natl. Acad. Sci. USA* **116**, 1526 (2019).
- [34] B. B. Iversen, A. E. C. Palmqvist, D. E. Cox, G. S. Nolas, G. D. Stucky, N. P. Blake, and H. Metiu, *J. Solid State Chem.* **149**, 455 (2000).
- [35] T. Takabatake, K. Suekuni, T. Nakayama, and E. Kaneshita, *Rev. Mod. Phys.* **86**, 669 (2014).
- [36] T. Kume, F. Ohashi, and S. Nonomura, *Jpn. J. Appl. Phys.* **56**, 05DA05 (2017).
- [37] J.-A. Dolyniuk, B. O. Baird, J. Wang, J. V. Zaikina, and K. Kovnir, *Mater. Sci. Eng., R* **108**, 1 (2016).
- [38] J. Gryko, P. F. McMillan, R. F. Marzke, G. K. Ramachandran, D. Patton, S. K. Deb, and O. F. Sankey, *Phys. Rev. B* **62**, R7707 (2000).
- [39] A. M. Guloy, R. Ramlau, Z. Tang, W. Schnelle, M. Baitinger, and Y. Grin, *Nature (London)* **443**, 320 (2006).
- [40] S. Christensen, L. Bjerg, A. Kaltzoglou, F. Juranyi, T. Fassler, T. Unruh, and M. Christensen, *J. Appl. Phys.* **113**, 084902 (2013).
- [41] J. Yuhara, Y. Fujii, K. Nishino, N. Isobe, M. Nakatake, L. Xian, A. Rubio, and G. L. Lay, *2D Mater.* **5**, 025002 (2018).
- [42] P. Sadhukhan, S. Barman, T. Roy, V. K. Singh, S. Sarkar, A. Chakrabarti, and S. R. Barman, *Phys. Rev. B* **100**, 235404 (2019).
- [43] P. Sadhukhan, D. Pandey, V. K. Singh, S. Sarkar, A. Rai, K. Bhattacharya, A. Chakrabarti, and S. R. Barman, *Appl. Surf. Sci.* **506**, 144606 (2020).
- [44] V. A. Rogalev, F. Reis, F. Adler, M. Bauernfeind, J. Erhardt, A. Kowalewski, M. R. Scholz, L. Dudy, L. B. Duffy, T. Hesjedal, M. Hoesch, G. Bihlmayer, J. Schafer, and R. Claessen, *Phys. Rev. B* **100**, 245144 (2019).
- [45] M. Liao, Y. Zang, Z. Guan, H. Li, Y. Gong, K. Zhu, X.-P. Hu, D. Zhang, Y. Xu, Y.-Y. Wang, K. He, X.-C. Ma, S.-C. Zhang, and Q.-K. Xue, *Nat. Phys.* **14**, 344 (2018).
- [46] D. D. Sante, P. Eck, M. Bauernfeind, M. Will, R. Thomale, J. Schäfer, R. Claessen, and G. Sangiovanni, *Phys. Rev. B* **99**, 035145 (2019).
- [47] Z. Shi, X. Wang, C. Xu, P. Wang, Y. Liu, and T.-C. Chiang, *Phys. Lett. A* **384**, 126782 (2020).
- [48] N. Si, Q. Yao, Y. Jiang, H. Li, D. Zhou, Q. Ji, H. Huang, H. Li, and T. Niu, *J. Phys. Chem. Lett.* **11**, 1317 (2020).
- [49] Y. Xu, B. Yan, H.-J. Zhang, J. Wang, G. Xu, P. Tang, W. Duan, and S.-C. Zhang, *Phys. Rev. Lett.* **111**, 136804 (2013).
- [50] V. K. Singh, M. Mihalkovič, M. Krajić, S. Sarkar, P. Sadhukhan, M. Maniraj, A. Rai, K. Pussi, D. L. Schlagel, T. A. Lograsso, A. K. Shukla, and S. R. Barman, *Phys. Rev. Res.* **2**, 013023 (2020).
- [51] A.-P. Tsai, A. Inoue, and T. Masumoto, *Mater. Trans., JIM* **30**, 463 (1989).
- [52] K. Hiraga, W. Sun, and A. Yamamoto, *Mater. Trans., JIM* **35**, 657 (1994).
- [53] A. Yamamoto and S. Weber, *Phys. Rev. Lett.* **79**, 861 (1997).
- [54] K. Sugiyama, S. Nishimura, and K. Hiraga, *J. Alloys Compd.* **342**, 65 (2002).
- [55] M. Krajić, J. Hafner, and M. Mihalkovič, *Phys. Rev. B* **73**, 134203 (2006).
- [56] V. Fournée, A. R. Ross, T. A. Lograsso, J. W. Evans, and P. A. Thiel, *Surf. Sci.* **537**, 5 (2003).
- [57] W. R. Tyson and W. A. Miller, *Surf. Sci.* **62**, 267 (1977).
- [58] M. Shimoda, J. Guo, T. Sato, and A.-P. Tsai, *J. Non-Cryst. Solids* **334–335**, 505 (2004).
- [59] C. A. Schneider, W. S. Rasband, and K. W. Eliceiri, *Nat. Methods* **9**, 671 (2012).
- [60] I. R. Fisher, M. J. Kramer, Z. Islam, A. R. Ross, A. Kracher, T. Wiener, M. J. Sailer, A. I. Goldman, and P. C. Canfield, *Philos. Mag. B* **79**, 425 (1999).
- [61] P. C. Canfield, *Rep. Prog. Phys.* **83**, 016501 (2020).
- [62] V. K. Singh and S. R. Barman, in *DAE Solid State Physics Symposium 2019*, edited by V. K. Sharma, C. L. Prajapat, and S. M. Yusuf, AIP Conf. Proc. 2265 (AIP, Melville, NY, 2020), p. 030311.
- [63] A. K. Shukla, S. Banik, R. S. Dhaka, C. Biswas, S. R. Barman, and H. Haak, *Rev. Sci. Instrum.* **75**, 4467 (2004).
- [64] G. Kresse and J. Furthmüller, *Phys. Rev. B* **54**, 11169 (1996).
- [65] G. Kresse and D. Joubert, *Phys. Rev. B* **59**, 1758 (1999).
- [66] J. P. Perdew, J. A. Chevary, S. H. Vosko, K. A. Jackson, M. R. Pederson, D. J. Singh, and C. Fiolhais, *Phys. Rev. B* **46**, 6671 (1992).

- [67] See Supplemental Material at <http://link.aps.org/supplemental/10.1103/PhysRevB.107.045410> for Figs. S1–S9, Tables SI–III, a note, three CONTCAR files, and seven video files.
- [68] H. R. Sharma, K. J. Franke, W. Theis, A. Riemann, S. Fölsch, P. Gille, and K. H. Rieder, *Phys. Rev. B* **70**, 235409 (2004).
- [69] T. Haibach, A. Cervellino, M. A. Estermann, and W. Steurer, *Philos. Mag. A* **79**, 933 (1999).
- [70] A. Rai, V. K. Singh, J. Nayak, and S. R. Barman, *Surf. Sci.* **679**, 169 (2019).
- [71] K. Heinz, *Rep. Prog. Phys.* **58**, 637 (1995).
- [72] R. D. Diehl, Th. Seyller, M. Caragiu, G. S. Leatherman, N. Ferralis, K. Pussi, P. Kaukasoina, and M. Lindroos, *J. Phys.: Condens. Matter* **16**, S2839 (2004).
- [73] K. Pussi, N. Ferralis, M. Mihalkovič, M. Widom, S. Curtarolo, M. Gierer, C. J. Jenks, P. C. Canfield, I. R. Fisher, and R. D. Diehl, *Phys. Rev. B* **73**, 184203 (2006).
- [74] S. Sarkar, S. Barman, M. Balal, and S. R. Barman, *Appl. Surf. Sci.* **563**, 150067 (2021).
- [75] H. R. Sharma, J. A. Smerdon, P. J. Nugent, A. Ribeiro, I. McLeod, V. R. Dhanak, M. Shimoda, A.-P. Tsai, and R. McGrath, *J. Chem. Phys.* **140**, 174710 (2014).
- [76] M. Engel, P. F. Damasceno, C. L. Phillips, and S. C. Glotzer, *Nat. Mater.* **14**, 109 (2015).
- [77] J. Vuorinen, K. Pussi, R. D. Diehl, and M. Lindroos, *J. Phys.: Condens. Matter* **24**, 015003 (2012).
- [78] M. O’Keefe, G. B. Adams, and O. F. Sankey, *Philos. Mag. Lett.* **78**, 21 (1998).
- [79] M. Mihalkovič, J. Richmond-Decker, C. L. Henley, and M. Oxborrow, *Philos. Mag.* **94**, 1529 (2014).
- [80] E. Pospíšilová and M. Mihalkovič (unpublished).
- [81] N. G. Hörmann, A. Gross, J. Rohrer, and P. Kaghazchi, *Appl. Phys. Lett.* **107**, 123101 (2015).
- [82] J. Ledieu, M. Krajčí, J. Hafner, L. Leung, L. H. Wearing, R. McGrath, T. A. Lograsso and D. Wu, V. Fournée, *Phys. Rev. B* **79**, 165430 (2009).
- [83] J. A. Smerdon, J. K. Parle, L. H. Wearing, T. A. Lograsso, A. R. Ross, and R. McGrath, *Phys. Rev. B* **78**, 075407 (2008).
- [84] M. Maniraj, A. Rai, and S. R. Barman, M. Krajčí, D. L. Schlage, T. A. Lograsso, and K. Horn, *Phys. Rev. B* **90**, 115407 (2014).
- [85] For W-Al-Ni-Co, the lattice parameters optimized by DFT are by factor 0.9975 shorter than the experimental lattice. The fundamental  $\alpha$ -Sn structure yields optimized lattice parameters by 1.023 factor longer than the experiment. The DFT lattice mismatch computed for the R<sub>2</sub>T<sub>4</sub> approximants of the Sn clathrate versus *d*-Al-Ni-Co is 1.033. Thus, our extrapolated realistic mismatch estimate is  $1.033/1.023 \times 0.9975 = 1.007$ .
- [86] M. Mihalkovič and M. Widom, *Phys. Rev. Res.* **2**, 013196 (2020).
- [87] M. Mihalkovič and C. L. Henley, *Phys. Rev. B* **85**, 092102 (2012).
- [88] L.-H. Ye, *Phys. Rev. B* **92**, 115132 (2015).
- [89] A. E. Madison, *Phys. Solid State* **56**, 1706 (2014).
- [90] H. Takakura, C. P. Gomez, A. Yamamoto, M. D. Boissieu, and A. P. Tsai, *Nat. Mater.* **6**, 58 (2007).
- [91] M. Krajčí and J. Hafner, in *Quasicrystals*, Series in Handbook of Metal Physics, edited by T. Fujiwara and Y. Ishii (Elsevier, Amsterdam, 2008), Vol. 2, Chap. 9, pp. 313–355.
- [92] A. P. Tsai and C. Cui, in *Handbook of Crystal Growth*, edited by T. Nishinaga (Elsevier, Amsterdam, 2015), Chap. 26, pp. 1113–1156.
- [93] N. D. Lang and W. Kohn, *Phys. Rev. B* **1**, 4555 (1970).